

Comparison of the neutron, Raman, and infrared vibrational spectra of vitreous SiO₂, GeO₂, and BeF₂

F. L. Galeener

Xerox Palo Alto Research Centers, Palo Alto, California 94304

A. J. Leadbetter

Chemistry Department, University of Exeter, Exeter EX4 4QD, Great Britain

M. W. Stringfellow

Atomic Energy Research Establishment, Harwell, Didcot, Oxon OX11 0RA, Great Britain

(Received 30 August 1982)

The inelastic neutron, Raman, and infrared vibrational spectra of vitreous SiO₂, GeO₂, and BeF₂ are reported in detail and compared with one another. The neutron spectrum is shown to be a good measure of the vibrational density of states for glassy SiO₂ and GeO₂, but a poorer measure for BeF₂. The density of states is shown to be split into transverse-optical—longitudinal-optical bands whose nature is revealed in the infrared and Raman spectra. Empirical selection rules are noted, including the observation that the *HV* Raman spectrum “mimics” the density of states, while the *HH* spectrum is dominated by matrix-element effects. The spectra are discussed in terms of an augmented central-force model which allows prediction of selection rules and relative densities of states. The latter allows an empirical estimate of the frequency dependence of the neutron scattering coupling coefficients, showing relatively weak scattering by acoustic modes, especially in the case of BeF₂ glass.

I. INTRODUCTION

Considerable progress has recently been made in understanding the vibrational properties of amorphous materials,^{1–11} especially the infrared (ir) and Raman spectra.^{7–11} Since the pioneering computational work of Bell, Dean, and co-workers,^{8–25} further significant insights into the nature of the vibrations have been provided by a rather simple analytical description introduced by Sen and Thorpe,^{26–28} based essentially only on local order and nearest-neighbor central forces.

While the Raman and ir spectra provide great insight into the character of modes in different frequency regimes, they do not provide a very direct measure of the vibrational density of states (VDOS), $\rho(\omega)$. This is because the coupling coefficients or matrix elements linking these optical spectra with the VDOS are not easily obtained,^{29–35} and are sometimes strong functions of vibrational frequency ω .^{33–35} Previous inelastic neutron scattering studies of glasses by Leadbetter and co-workers,^{36–40} including polycrystalline and vitreous silica,³⁹ indicated that inelastic neutron scattering gives a rather direct measure of $\rho(\omega)$, at least for $\omega > 250 \text{ cm}^{-1}$. In particular, the neutron coupling coefficients were

estimated to be slowly varying functions of frequency,³⁹ using the results of model calculations of Bell and co-workers.^{13–17}

In Sec. II of this paper, we therefore report inelastic neutron scattering measurements on polycrystalline and vitreous (*v*-) modifications of GeO₂ and BeF₂ and, for these substances as well as for SiO₂, we show that crystal and vitreous data are very closely similar. This is a striking result which shows that $\rho(\omega)$ is very insensitive to the details of the long-range order. This conclusion is reinforced by noting that the crystal data used in the comparison are for the quartz-crystal modification, which is not the crystal form having a topology of tetrahedral packing closest to that of the glass.^{41,42} The neutron estimates of the one-phonon VDOS are then compared with the numerical predictions of Bell and Dean.¹⁸ We note that their model calculations give broadly correct results, except for the use of inappropriate non-central-force constants for *v*-GeO₂ and *v*-BeF₂, and neglect of long-range Coulombic effects.

Since a major object of this paper is to compare Raman and infrared with neutron results, we present in Sec. III a full summary of the experimental “optical” data. This includes an intercomparison of Ra-

man and infrared spectra which reveals the existence of splittings due to long-range electromagnetic forces.

In Sec. IV we outline the nearest-neighbor central-force (NN-CF) model and apply it to the optical spectra. A principal result is to conclude that there must be strong matrix-element effects in Raman scattering, and that the dominant Raman line marks the position of a relatively small number of "symmetric stretch" modes, whose frequency is easily predicted by the NN-CF model.

In Sec. V we compare the neutron, Raman, and ir spectra. In each case, this is carried out in terms of suitably reduced experimental spectra $S(\omega)$. The reduced optical spectra are directly related to subbands b in the VDOS in the form

$$S(\omega) = \sum_b C_b(\omega) \rho_b(\omega). \quad (1)$$

The subscript b denotes bands containing vibrations of similar mode type. Several of these subbands may contribute in a given frequency range (i.e., overlap), and the total VDOS is given by

$$\rho(\omega) = \sum_b \rho_b(\omega). \quad (2)$$

This division into separate bands was first done by Shuker and Gammon^{29,30} and is especially important for the optical experiments where the coupling coefficients $C_b(\omega)$ for the individual bands are expected to vary greatly from band to band. The $C_b(\omega)$ will be weaker functions of frequency than an overall coupling coefficient $C(\omega)$ defined by the relation

$$S(\omega) \equiv C(\omega) \rho(\omega). \quad (3)$$

For inelastic neutron scattering, the coupling coefficients are expected to vary little from band to band, and it is simpler to begin with a relation of the form of Eq. (3). Much is learned in Sec. V from comparison of the various spectra for the three materials without reference to microscopic models. Among

these empirical "selection rules" are the observations that: (1) the HV polarized Raman spectrum "mimics" the VDOS while the HH spectrum does not, (2) the high-frequency ir data mimic the VDOS while the low frequency do not, and (3) the TO-LO lines in the Raman spectra correspond to distinct separate bands in the VDOS. [A spectrum mimics the VDOS if the C_b in Eq. (1) are independent of frequency.]

The results are further discussed in Sec. VI in terms of a NN-CF model "augmented" by rocking and acoustic modes at lower frequencies. This enables extraction of the central- (α) and non-central- (β) force constants, as well as an empirical study of the distribution of numbers of states amongst the observed bands. Finally, we obtain from this an encouraging empirical estimate of the frequency dependence of the neutron coupling coefficients.

We are thus able to understand in a semiquantitative manner the general form of $\rho(\omega)$ and most of the neutron, Raman, and ir coupling coefficients. The most difficult problems remain at the lowest frequencies ($\omega < 250 \text{ cm}^{-1}$), where acoustic modes appear together with modes which are dominated by bond-bending forces and are also sensitive to the longer-range structural configuration.

II. NEUTRON SCATTERING SPECTRA

A. Amorphous and crystalline samples

For all three materials, neutron scattering measurements were made on both the glass and the polycrystalline-quartz modification. The neutron scattering samples all had slab geometry, and were held in parallel-sided containers with aluminum-foil windows. The glass was in the form of sheets and the crystals were of particle size $< 100 \mu\text{m}$. The sample thicknesses used are listed in Table I.

The silica-glass sample was composed of sheets of electrically fused quartz (Thermal Syndicate Ltd., ir-grade Vitreosil), and the crystalline specimen was

TABLE I. Specimen thicknesses for neutron scattering.

Substance	Form	Thickness (g cm^{-2})
SiO ₂	Glass	2.65
	Quartz crystals	2.59
GeO ₂	Glass	1.55
	Quartz crystals	0.71 (dry), 1.58 (wet)
BeF ₂	Glass	0.89
	Quartz crystals	1.17

prepared by crushing synthetic α -quartz single crystals.

The polycrystalline-quartz modification of GeO_2 used was a 99.999%-pure material from Koch Light Ltd. As will be shown below, the first sample examined contained an appreciable amount of sorbed water which was revealed as an anomalously high neutron scattering cross section. This water was removed in a subsequent experiment by heat treatment at 700°C . The GeO_2 glass was made from similar starting material by melting at 1590°C in a platinum crucible, fining at 1500°C , and annealing at 520°C .

The BeF_2 starting material was anhydrous crystalline powder supplied by the Gallard Schlesinger Chemical Corp. The glass specimen was made by melting this material at 850°C in a gold-foil-lined silica vessel, fining at 600°C , and annealing at 140°C . The quartz modification was made by devitrifying the actual glass sample used for the neutron scattering experiments by heating for four days at 400°C . The neutron specimen was prepared by grinding the devitrified mass in a P_2O_5 dry box. X-ray diffraction measurements confirmed that the product was good-quality quartz-structure crystal.

B. Be filter spectroscopy

The inelastic neutron scattering measurements were made at the Atomic Energy Research Establishment (AERE), Harwell, using the beryllium filter spectrometer on the PLUTO reactor. In this instrument,⁴³ monoenergetic neutrons are obtained from a crystal monochromator and scattered by the sample through a liquid-nitrogen-cooled filter of polycrystalline beryllium into a bank of BF_3 counters. The upper energy limit to the transmission of the filter is 42 cm^{-1} , and the response of filter and counters is such that the mean energy of detected neutrons is 26 cm^{-1} . By varying the monochromator takeoff angle, the incident neutron energy may be varied up to a useful maximum of about 1400 cm^{-1} , determined by the flux of the thermal beam. Higher-order contamination of the incident beam at low energies provides an effective lower limit to the incident energy of about 120 cm^{-1} . For low energies, the incident beam was obtained by reflection from the $\{111\}$ planes of an aluminum monochromator while, for intermediate and high energies, the $\{311\}$ and $\{511\}$ planes, respectively, were used. The overall energy resolution was better than 10% over the whole energy range.

The scattering was observed in symmetrical transmission geometry with a scattering angle of 80° , and all measurements were made at an ambient temperature $\sim 20^\circ\text{C}$. To correct for various sources of background, counts were made at each energy

with all four possible combinations of the conditions: (1) the monochromator set at, or offset from, the Bragg condition, and (2) the specimen in or out of the beam. From these four measurements, the true scattering of the monoenergetic beam by the specimen was deduced.

C. Data reduction

Given the sensitivities of the incident beam monitor and detector system, the double-differential scattering cross section $d^2\sigma/d\Omega dE$ may be obtained directly from the experimental measurements. However, we are interested primarily in the vibrational frequency distribution of $\rho(\omega)$, and it is then more useful to show the experimental data in the form of the experimental function $G(Q, \omega)$, which is related to the differential cross section by the equation

$$G(Q, \omega) = (k_0/k)(2\omega/Q^2) \times [n(\omega) + 1]^{-1} \frac{d^2\sigma}{d\Omega dE}, \quad (4)$$

where k and k_0 are, respectively, the scattered and incident neutron wave vectors, and $n(\omega)$ is the Bose-Einstein population factor for vibrations of frequency ω .

The significance of this function is that, for one-phonon incoherent scattering by a monatomic specimen, $G(Q, \omega)$ is simply the amplitude-weighted frequency distribution.⁴⁴ For polyatomic coherent scatterers, like the substances investigated here, then in the incoherent approximation, and provided that atoms of the same chemical species may be assumed to be dynamically equivalent, it has been shown elsewhere^{38,39} that

$$G(Q, \omega) = A(Q, \omega)[\rho(\omega) + \rho_2(\omega) + \dots], \quad (5)$$

where

$$A(Q, \omega) = \sum_I M_I^{-1} \langle b_I^2 \rangle \langle \xi_I^2(\omega) \rangle e^{-2W_I(Q)} \quad (6)$$

and $\rho_2(\omega)$ is the two phonon term, etc. The neutron coupling coefficient $A(Q, \omega)$ is dependent on Q through the exponential Debye-Waller factor, where $W_I(Q) = Q^2 \langle U_I^2 \rangle$. Here M_I is the mass of atom I , $4\pi \langle b_I^2 \rangle$ its total neutron scattering cross section, and $U_I(\omega)$ its displacement. The sum is over all atoms I in a formula unit, while $\langle \xi_I^2 \rangle$ denotes the mean-square polarization vector of atom I over modes in the neighborhood of ω .

The incoherent approximation is valid for values of Q such that $Q > 2\pi/r_1$ where r_1 is the nearest-neighbor distance. For the present experiment $Q \simeq k_0$, so this condition becomes $\lambda_0 < r_1$, meaning

that the incoherent approximation should be valid for incident energies greater than about 250 cm^{-1} . This is consistent with the results of cold neutron scattering experiments on these substances,³⁶⁻³⁸ which showed significant coherence effects only for energy transfers less than about 300 cm^{-1} .

D. Neutron scattering results

The experimental results, expressed in terms of the function $G(Q, \omega)$, are shown in Figs. 1-3 for all the specimens. Following practice in Raman and ir spectroscopy, the data are presented in terms of the wave-number equivalent W of the phonon frequency ω , where $W(\text{cm}^{-1}) = 5.31 \times 10^{-12} \omega(\text{rad/sec})$. The

scale of $G(Q, \omega) \equiv G(Q, W)$ is arbitrary but, for each substance, the results for the glass and crystal forms are normalized to the same amount of substance.

For silica and beryllium fluoride, the area under the $G(Q, \omega)$ curve is closely similar for crystal and glass. For crystalline germania, the first experiment using the powder as supplied by the manufacturer gave $G(Q, \omega)$ values about a factor of 3 larger than for the glass. This sample (of unknown surface area) was shown by infrared spectroscopy to contain a significant amount of water, presumably adsorbed on the surface. The experiment was, therefore, repeated using a specimen which had been heat treated at 700°C . The area under the resulting $G(Q, \omega)$ curve was very similar to that for the glass, supporting our hypothesis that the anomalously high cross

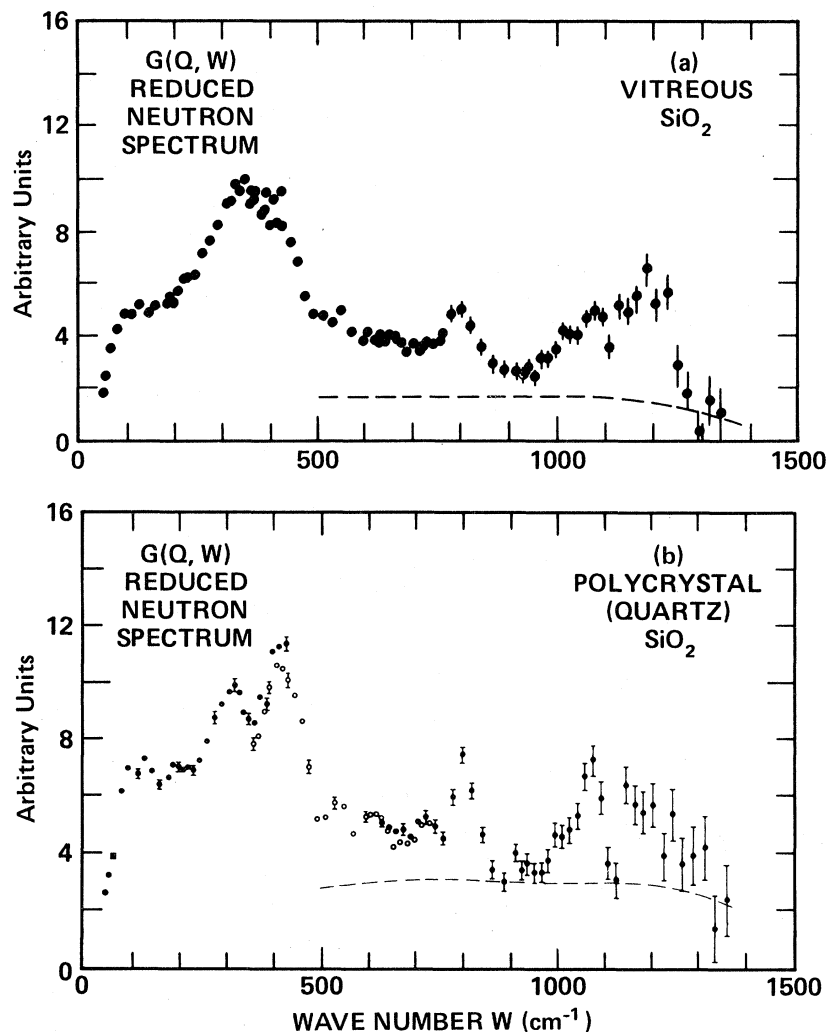


FIG. 1. Reduced neutron spectra $G(Q, W)$ measured for (a) vitreous SiO_2 and (b) α -quartz—structure crystalline SiO_2 powder. The dashed lines are estimates of two-phonon contributions according to Eq. (8). Note the strong similarity of these experimental estimates of the vibrational density of states for glass and crystal.

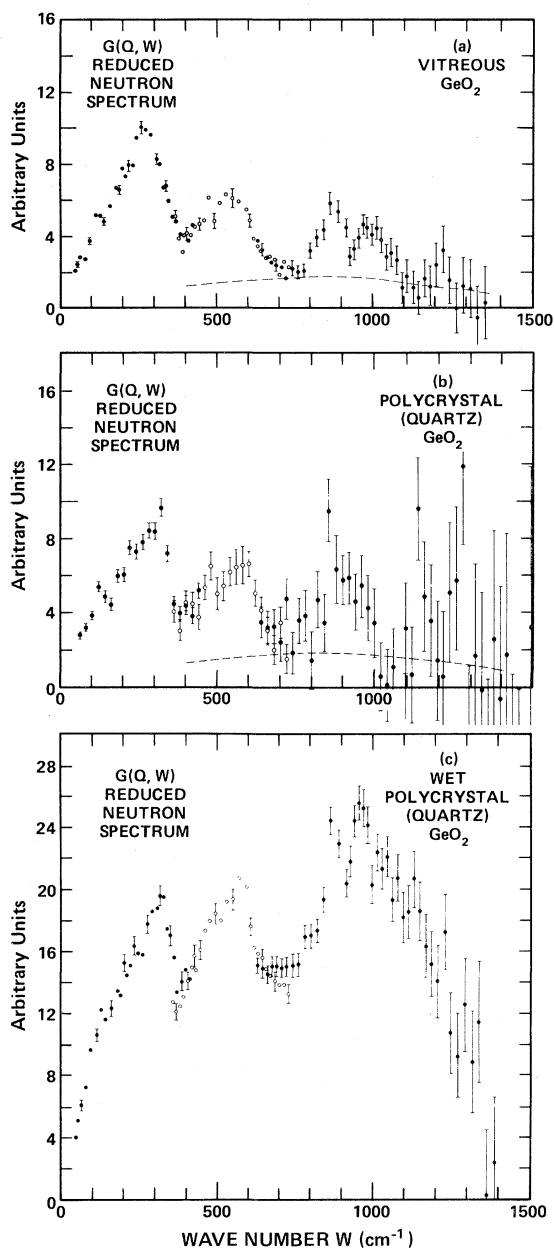


FIG. 2. Reduced neutron spectra $G(Q, W)$ measured for (a) vitreous GeO_2 , (b) α -quartz—structure crystalline GeO_2 powder, and (c) wet α -quartz GeO_2 powder. Note the increased cross section (and modified high-frequency bands) in (c) due to hydrogen in the adsorbed OH units. Also note the similarity of the $G(Q, W)$ estimate of the total vibrational density of states for glass and crystal, especially in the range 0–700 cm^{-1} .

section of the first specimen was due to adsorbed water. The amount of water required to account for the observed cross section is about 10^{-2} g per gram of GeO_2 . This surface water amplifies the scattering

intensity from the GeO_2 modes with a frequency-dependent amplification factor and gives rise to additional scattering which tends to fill in the troughs near 400 and 700 cm^{-1} . This is the general frequency region for water vibrations but, as no strong peaks are found in the additional scattering, no conclusions are possible about the state of the sorbed water.

Figures 1–3 show that for all three substances, $G(Q, \omega)$ for the glass is very similar indeed to that for the quartz-crystal modification. The coupling coefficients $A(Q, \omega)$ and the multiphonon scattering cannot differ greatly between crystal and glass, so this means that the frequency distributions themselves are closely similar for glass and crystal. Indeed, within the experimental uncertainty, especially that due to the poor statistics for crystalline GeO_2 at high energies (resulting from less material and shorter counting times), the glass results differ from those for the crystal only by a slight broadening of the peaks. Similar behavior is particularly noticeable for SiO_2 where the crystal data contain a good deal of structure.

This result is particularly striking because of the structural relation between the two forms. In all cases, the structure is based on an AX_4 tetrahedron, but the arrangement of the tetrahedra in the glasses does not closely resemble that in the quartz modifications, where the mass density^{41,42} is considerably higher. The density of the glass structure ($\rho \sim 2.2 \text{ g cm}^{-3}$) is in general much closer to that of the cristobalite (or perhaps tridymite) structure ($\rho \sim 2.3 \text{ g cm}^{-3}$) than to α -quartz ($\rho \sim 2.65 \text{ g cm}^{-3}$). The similarities in the frequency spectra between crystal and glass clearly show that, at least for $\omega > 200 \text{ cm}^{-1}$, $\rho(\omega)$ is dominated by the short-range aspects of the structure. The similarity between glass and crystal means, of course, that a detailed understanding of $\rho(\omega)$ for the crystal should enable one to predict $\rho(\omega)$ for the glass. To model the crystal, however, is far from easy, and we shall adopt the reverse viewpoint that the first important task is to try and understand the vibrational properties of a given substance which has a given local structure, the VDOS being to first approximation independent of the nature and extent of long-range order. We shall not, therefore, base our discussions of vibrations on any given crystal approach but rather on recent theoretical developments which utilize only the very-short-range properties of the structure.

In Secs. V and VI, the above results will be used in comparisons with optical spectra and model calculations. For this purpose, it is more convenient to use smooth curves rather than the raw point-by-point results. In Fig. 4, therefore, we show the con-

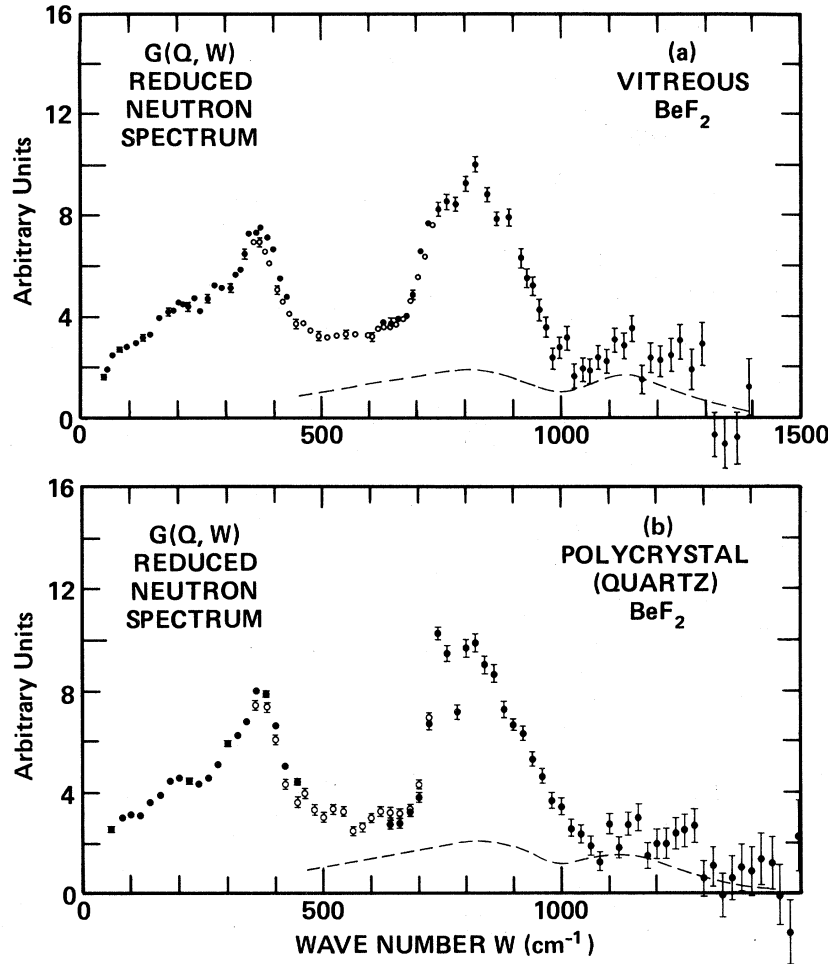


FIG. 3. Reduced neutron spectra $G(Q, W)$ measured for (a) vitreous BeF_2 and (b) α -quartz—structure crystalline BeF_2 powder. Note again that these experimental estimates of the total vibrational density of states are nearly identical in glass and crystal.

struction from the experimental results of the smoothed curves which will be used subsequently.

E. Estimation of the two-phonon contributions

According to Eq. (5) $G(Q, \omega)$ is the product of the functions $A(Q, \omega)$ and $[\rho(\omega) + \rho_2(\omega) + \dots]$. It is not possible to obtain $\rho(\omega)$ itself directly from experiment, since we have no experimental knowledge of the ξ_l^2 appearing in $A(Q, \omega)$. However, it is possible to make a reasonable experimental estimate of $\rho_2(\omega)$, the two-phonon contribution to $G(Q, \omega)$, and

$$\rho_2 = \frac{[n(\omega) + 1]\omega\omega_0}{2\mu} \int_{-\infty}^{\infty} \frac{\rho(\omega)\rho(\omega - \omega')d\omega'}{\omega(\omega - \omega')[1 - \exp(-\hbar\omega'/k_B T)][1 - \exp(-\hbar(\omega - \omega')/k_B T)]}, \quad (8)$$

with

also to calculate $A(Q, \omega)$ for certain models.

In order to circumvent the principal difficulty arising from the presence of two atom types with different scattering lengths and frequency-dependent relative displacements, we use a monatomic approximation³⁹ in which we take

$$G(Q, \omega) \sim \langle b^2 \rangle M^{-1} \{ \rho(\omega) \exp[-2W(Q)] + \rho_2(\omega) \}, \quad (7)$$

where the omission of the Debye-Waller term from $\rho_2(\omega)$ takes rough account of higher-order contributions. Here

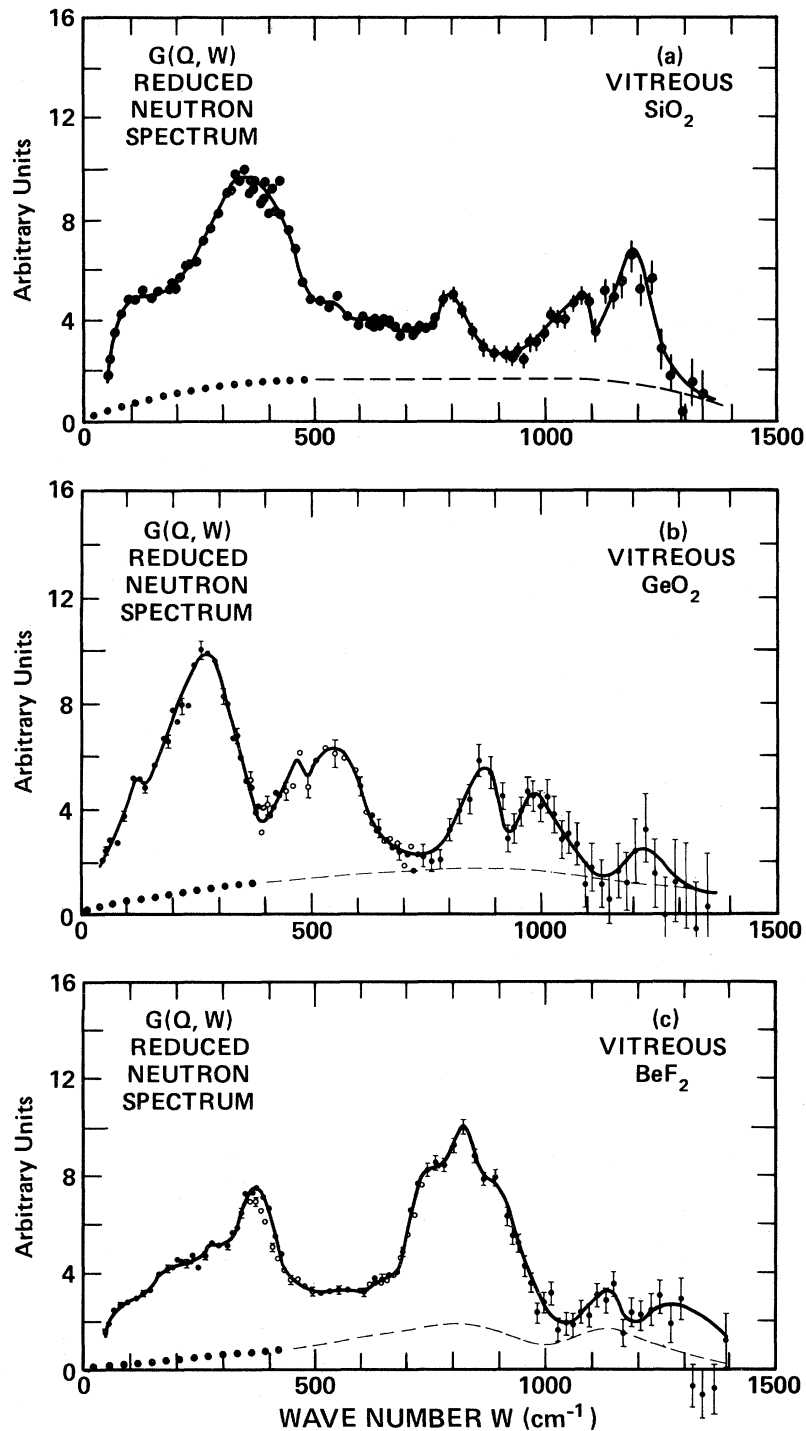


FIG. 4. Smooth curves are shown to be used henceforth to represent the points measured for $G(Q, W)$ in (a) v - SiO_2 , (b) v - GeO_2 , and (c) v - BeF_2 . Also shown (dotted lines) are smooth extensions of the estimated two-phonon contributions (dashed lines) to the origin at $W=0$. The two-phonon contributions are estimated according to Eq. (8) and cannot be considered to be exact. Owing to poor signal-to-noise ratio, the peaks above $W \sim 1100 \text{ cm}^{-1}$ in v - GeO_2 and v - BeF_2 may be spurious. Also suspect are the sharp peaks at ~ 125 and $\sim 475 \text{ cm}^{-1}$ in v - GeO_2 .

$$\mu^{-1} = \sum_I p_I \mu_I^{-1} M_I^{-1} \langle b_I^2 \rangle / \sum_I p_I M_I^{-1} \langle b_I^2 \rangle,$$

and where $\hbar\omega_0$ is the incident neutron energy, μ_I is the ratio of atomic mass to neutron mass, and p_I is the fraction of atoms of type I .

Analysis of the model calculations of Bell and co-workers¹³⁻¹⁷ (see below), shows that $A(Q, \omega)$ is not a strongly varying function of ω , and it was therefore assumed constant in calculating the two-phonon term. The latter was obtained from Eqs. (7) and (8) using an iterative procedure, and the results are shown as dashed lines in Figs. 1-3. The dotted lines in Fig. 4 are *ad hoc* extensions of the dashed lines to the origins. Although these calculations give only an approximate estimate of the multiphonon contribution, we feel entitled to conclude that all the scattering for $\omega > 1100 \text{ cm}^{-1}$ for GeO_2 and BeF_2 and $\omega > 1300 \text{ cm}^{-1}$ for SiO_2 is, in fact, multiphonon scattering.

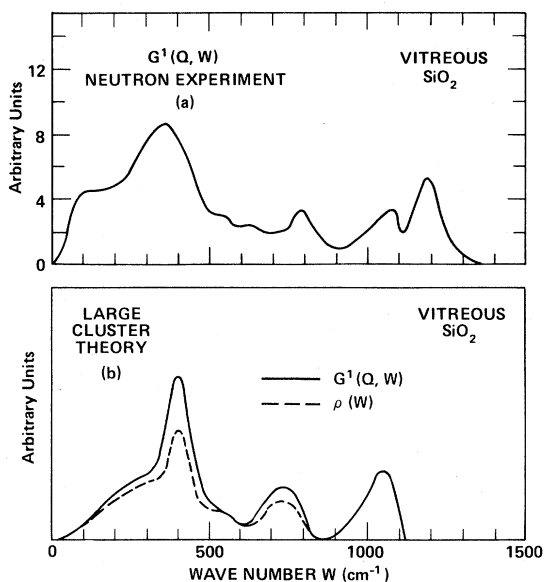


FIG. 5. (a) shows the experimental one-phonon reduced neutron scattering spectrum G^1 for $v\text{-SiO}_2$. G^1 is obtained by subtracting the two-phonon estimate from the experimental total $G(Q, W)$, as given in Fig. 4(a). (b) shows a theoretical vibrational density of states $\rho(W)$, as calculated for a large cluster with fixed-surface (oxygen) atoms by Bell and Dean (Ref. 18). The theoretical G^1 in (b) incorporates an estimate from the theory of the coupling coefficients $A(Q, W)$ in Eq. (5). Agreement between experimental and theoretical G^1 is encouraging as to the number and position of bands when one realizes that the theory omits the Coulomb forces that split the highest-frequency band into an observed TO-LO pair. There is noticeable disagreement in linewidths.

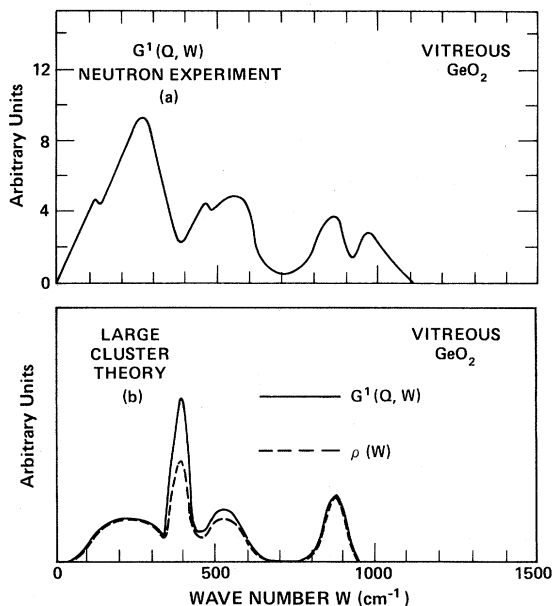


FIG. 6. (a) shows the experimental one-phonon reduced neutron scattering spectrum G^1 for $v\text{-GeO}_2$, where G^1 is obtained by subtracting the two-phonon estimate from the total $G(Q, W)$, both shown in Fig. 4(b). (b) shows theoretical values for the vibrational density of states $\rho(W)$ and for G^1 , based on calculations by Bell and Dean (Ref. 18) who treated a large cluster with fixed-surface (oxygen) atoms. The main discrepancies between the experimental and theoretical G^1 are the unpredicted TO-LO splitting of the highest-frequency band, discussed in Sec. III E, and the additional (sharp) band in $\rho(W)$ at about 400 cm^{-1} . The latter is ascribed in Sec. IV B to the use of excessively large noncentral forces in the theory.

F. The one-phonon contributions to $G(Q, \omega)$: Comparison with cluster theory

The estimated one-phonon components $G^1(Q, \omega)$ are found by subtracting the broken curves from the solid curves in Fig. 4. They are shown for the three glasses in Figs. 5-7 where they are compared with the calculated frequency distribution $\rho(\omega)$ of Bell and Dean,¹⁸ for fixed-surface atoms. In addition to $\rho(\omega)$ itself, Bell and Dean¹⁵ have also calculated as a function of frequency the proportion of the energy of the modes associated with the motions of the different atomic species. From these results, we are able to estimate for the model relative values of $\langle \xi_I^2(\omega) \rangle$ and $\langle U_I^2 \rangle$, hence $A(Q, \omega)$ and $G^1(Q, \omega) = A(Q, \omega)\rho(\omega)$, as was done by Leadbetter and Stringfellow.³⁹ The resultant values of $G^1(Q, \omega)$ for the model with fixed ends are shown in the lower panels of Figs. 5-7. These calculations indicate that $A(Q, \omega)$ is a slowly varying function of ω , the principal effect being merely to change the rel-

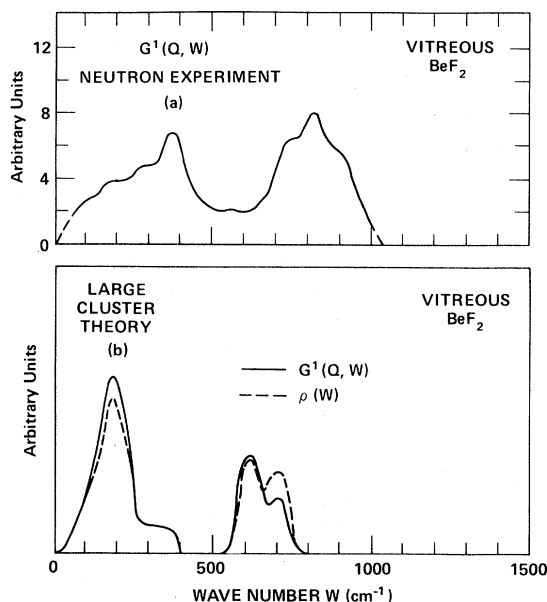


FIG. 7. (a) shows the experimental one-phonon reduced neutron scattering spectrum G^1 for v - BeF_2 , where G^1 is obtained by subtracting the two-phonon estimate from the total $G^1(Q, W)$, both shown in Fig. 4(c). (b) shows theoretical values based on the fixed-surface atom large-cluster calculations of Bell and Dean (Ref. 18). Quantitative agreement between theory and experiment is not good, except for the division into two groups of modes, and this is ascribed in Sec. IV B to use of excessively small noncentral forces in theory.

ative weights of peaks between $\rho(\omega)$ and $G^1(Q, \omega)$. The change is never greater than a factor of 2. The relative weights will be discussed in terms of the augmented central-force model in Sec. VI, where an empirical estimate will be deduced.

Model calculations were also made by Bell and co-workers,¹⁴⁻¹⁶ with the surface atoms free to vibrate. This results in additional modes appearing in regions of the spectrum where extra modes are, in fact, observed experimentally in the glass compared with the crystal (e.g., for $\omega \sim 900 \text{ cm}^{-1}$ for SiO_2), but the extra modes are too strong and sharply peaked in the model and for brevity are not shown in this paper.

For all three materials, the calculated frequency distribution $\rho(\omega)$ is in broad qualitative agreement with experiment. The same structural model was used in each case and included only simple central and noncentral forces for nearest-neighbor bonds, so this agreement confirms that the gross differences in shape between the spectra for the three substances are primarily due to the different mass ratios of the two atomic species. There are, of course, significant quantitative differences between model and experi-

ment which may be attributed first to the use of incorrect non-central-force constants. Galeener³⁴ has estimated from analysis of the optical spectra that, while the non-central-force constant value used for SiO_2 was good, those for GeO_2 and BeF_2 were, respectively, a factor of 2 too great and a factor of 2 too small. An improved estimate of the non-central-force constants will be given in Sec. V. The second major reason for the inadequacy of the model is its neglect of the effects of Coulombic interactions. Such effects are very well characterized in crystals: for example, the splitting of the highest-energy band in $\rho(\omega)$ for quartz into two components centered near 1080 and 1200 cm^{-1} is primarily a TO-LO splitting due to these interactions.⁴⁵⁻⁴⁷ It was recognized some time ago that this effect might carry over into the glass³⁹ and this has now been very clearly demonstrated in all three of the materials studied here.⁴⁸⁻⁵² We shall show in Sec. III E that clear TO-LO splittings have been identified in the optical spectra of the glasses, and in Sec. V that such splittings also affect $\rho(\omega)$ itself. This shows that any complete description of the VDOS of these materials must incorporate long-range electromagnetic forces.

III. RAMAN AND INFRARED SPECTRA

This section includes an expanded and unified presentation of results originally reported in two letters journals.^{48,50}

A. Glass samples for Raman and infrared spectroscopy

All samples were in the form of polished rectangular parallelepipeds at least 20 mm long, 10 mm wide, and 5 mm thick. This large size allowed the same sample to be used for both Raman scattering and infrared-reflectivity measurements. All samples were clear, colorless, and appeared to be bubble-free. They were well annealed so as to show no strain patterns between crossed polarizers.

The v - SiO_2 was bulk high-purity Suprasil W-1.⁵³ This material is known to have low OH content (< 5 ppm), low metallic impurity levels (total < 1 ppm), and extremely low (microscopic) bubble content. It is not noticeably hygroscopic, and the sample was continually exposed to room atmosphere. The Raman spectra of this material are essentially the same as those of the Vitreosil⁵⁴ used in the neutron scattering, apart from negligible effects due to different water content. The small effects of varying water content on Raman spectra have been reported elsewhere,⁵⁵⁻⁶⁰ as have those of varying thermal history,⁵⁶⁻⁵⁸ or fictive temperature.⁵⁸ In

short, the ν -SiO₂ samples used for all three spectroscopies may be taken as identical in structure.

The high-purity ν -GeO₂ was made at Bell Laboratories.⁶¹ This particular sample has very low OH content (< 5 ppm) and shows no bubbles under microscopic examination; the total level of metallic impurities appears to be quite low (absence of color and luminescence) but is not precisely known. The small effects of water content on the Raman spectra have been reported elsewhere⁵⁵ as have the effects of 10% excess Ge⁶² (a condition difficult to achieve). Again, we conclude that the ν -GeO₂ samples used for all three spectroscopies can be taken as having identical structure.

The ν -BeF₂ for optical studies was made by the same procedures (in the same laboratory) as the material used for neutron scattering, hence the structure can be taken as identical. Although colorless, the sample exhibited luminescence under laser excitation, suggesting a higher level of impurities than existed in the ν -SiO₂ and ν -GeO₂. Since the material is hygroscopic and toxic, the sample was polished in a dry box using disposable gloves, etc., then sealed in an evacuated quartz ampoule. Raman spectra were obtained with the sample still inside the ampoule, while ir reflection spectra were obtained with the sample removed from the ampoule and placed in a reflectivity chamber flushed with dry nitrogen gas.

B. Spectroscopic technique

Figure 8 shows schematically the arrangement used for obtaining polarized Raman spectra in the 90° scattering configuration. The laser was a CR-12 Ar⁺-ion laser whose output at wavelength λ_L was polarized as indicated by E_{in} in Fig. 8. The light scattered at 90° was collected by an $f/1$ lens and

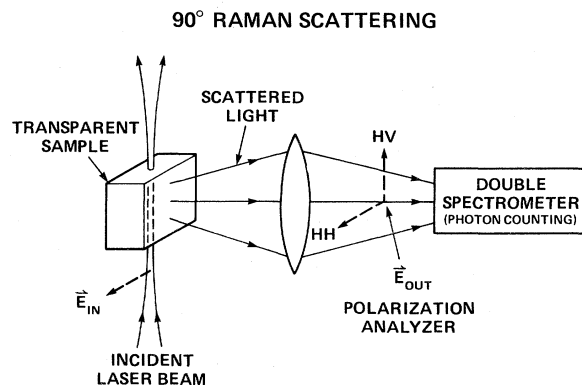


FIG. 8. Geometry of the Raman-scattering experiments reported in this paper, showing the polarization conventions HH and HV used herein.

passed through a polarization analyzer and polarization scrambler into a Spex 1401 double monochromator. Spectral slit width was set at 4 cm⁻¹. Detection was by means of an RCA 31034A GaAs photomultiplier and an SSR-1110 photon-counting system. Use of a reference channel effectively stabilized laser output to one part in 3000.⁵⁵ Pulses were counted for 10 sec at 5 cm⁻¹ intervals so that the peak signal-to-noise ratio was as high as 1000:1 in the spectra to be presented.

We label the spectrum HH when the scattered electric vector passed by the analyzer, \vec{E}_{out} , is parallel to \vec{E}_{in} ; the spectrum is HV when $\vec{E}_{out} \perp \vec{E}_{in}$, as shown in Fig. 8. A purely isotropic scatterer would give no spectrum in the HV configuration (in the electric dipole approximation). Thus the existence of HV scattering reveals the presence of anisotropic scattering (i.e., a contribution from off-diagonal elements in the Raman scattering tensor⁶³).

The ir reflectivity spectra were obtained using a Perkin-Elmer Model 180 spectrometer flushed with dry nitrogen and equipped with a dual-beam specular reflectance attachment. The spectral slit width was always less than 5 cm⁻¹. The radiation was focused on the sample, as shown schematically in Fig. 9. The angle of incidence of the center ray was 20° (from the normal) and the total spread of angles in the cone of radiation incident on the sample was ~20°. The incident ir radiation was unpolarized and all of the specularly reflected energy was detected (regardless of polarization). It is conventional to treat the results of such measurements as equivalent to normal-incidence data (which is not obtainable with commercial spectrometers), but the distinction should be kept in mind since reflectivity generally changes with the angle of incidence.⁶⁴

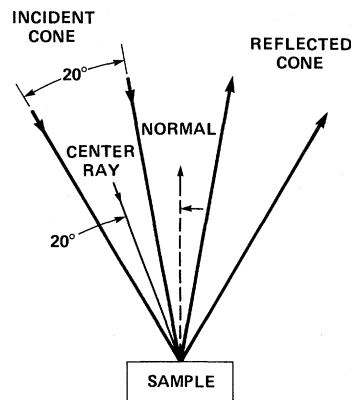


FIG. 9. Geometry of the infrared-reflectivity experiments reported in this paper, showing that the center ray is approximately 20° from normal incidence.

C. The measured Raman and infrared spectra

The polarized Raman spectra (a) and near-normal ir reflectivity spectra (b) are shown in Figs. 10–12, as measured. They are qualitatively similar, as befits materials thought to have similar network topology. The Raman spectra all show a single dominant rather broad and highly polarized line, whose origin has been identified³⁴ as due to symmetric-stretch (SS) motion of the bridging O (or F) atoms. The relative strengths of scattering by these materials are quite different, as has been elaborated elsewhere.⁶⁵ Two or three weaker, broad, but much less polarized lines are also seen at higher frequencies. The broad lines comprise the main features of the one-phonon Raman response of the glasses. Much weaker lines due to excitation of two phonons have been observed at higher frequencies,⁶⁶ but they are not of further interest in this paper.

The reflectivity spectra, obtained at 20° from normal incidence, are also qualitatively similar from material to material. Each glass shows two major bands, the stronger one is at higher frequencies and occurs in the same region as the weakly polarized Raman bands (1000–1300 cm^{-1} in ν - SiO_2). The latter characteristic has been described as showing “complementarity” in glasses, meaning that modes

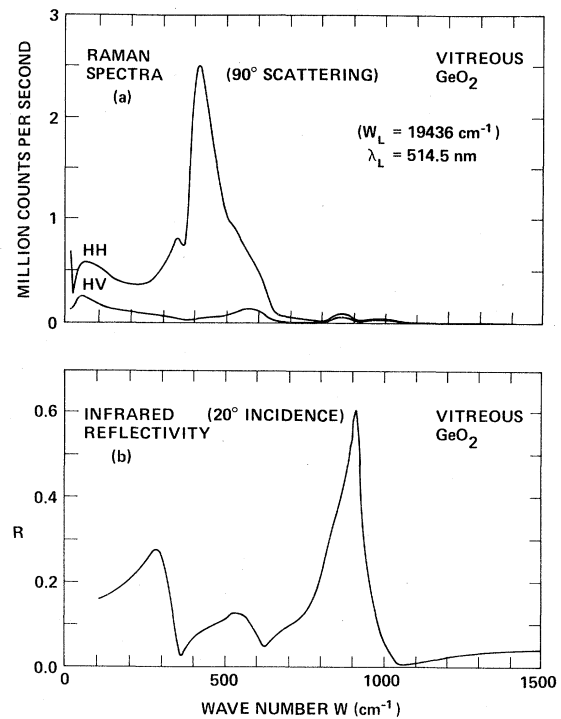


FIG. 11. Polarized Raman spectra (a) and near-normal (20°) infrared reflectivity (b) of ν - GeO_2 , taken at room temperature.

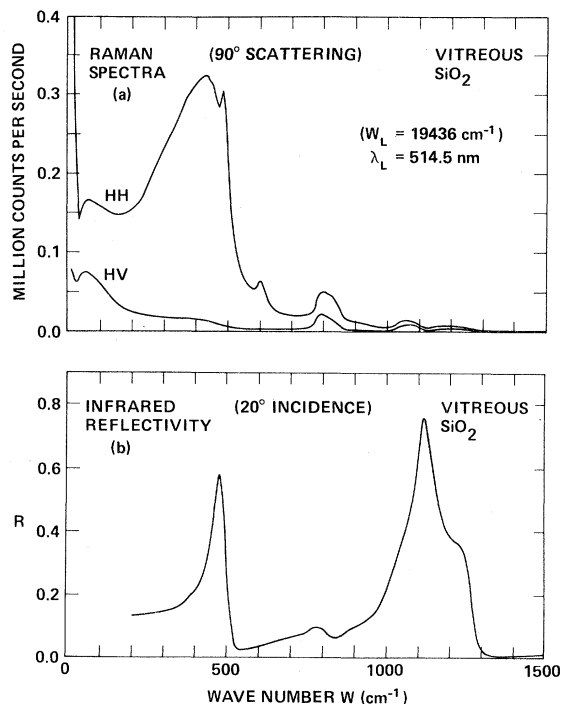


FIG. 10. Polarized Raman spectra (a) and near-normal (20°) infrared reflectivity (b) of ν - SiO_2 , taken at room temperature.

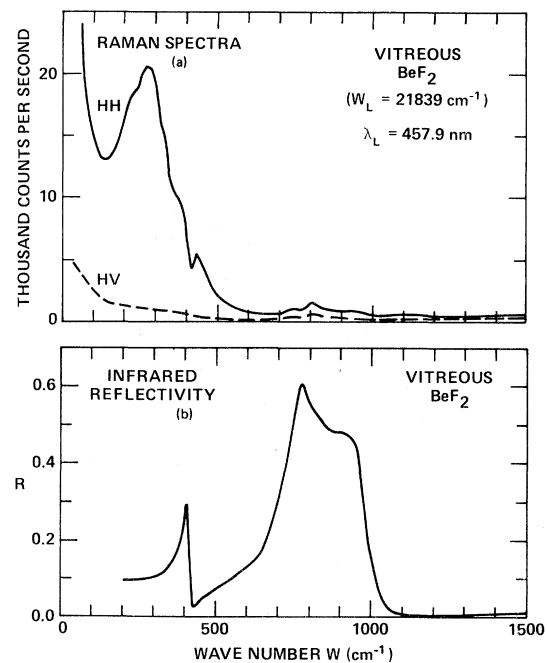


FIG. 12. Polarized Raman spectra (a) and near-normal (20°) infrared reflectivity (b) of ν - BeF_2 , taken at room temperature.

strong in infrared are weak in Raman, and vice versa. If one looks at the *HV* Raman spectra, however, complementarity is not observed, and more precise statements concerning selection rules are needed.

D. Data reduction

The raw spectra in Figs. 10–12 must be converted into other forms for meaningful comparison with each other, with the neutron spectra, and with the predictions of microscopic models for structure and vibrational response. For example, the Raman spectra are enhanced at low frequencies because at room temperature there is a greater population of thermally excited low-energy phonons with which to interact. One wants to remove extraneous temperature dependencies which give rise to spurious features, such as the “Bose” peak seen at about 50 cm^{-1} in *v*-SiO₂ and *v*-GeO₂. One also wants to put the data in a form suitable for direct comparison with $\rho(\omega)$, the VDOS obtained from neutron scattering experiments, or from vibrational theories.

Galeener and Sen³³ have derived very general expressions in the harmonic approximation, which relate the first-order Raman and ir spectra of a disordered solid to a common set of vibrational densities of states, or subbands $\rho_b(\omega)$. They have shown that Raman and ir spectra of disordered solids can be compared on an equivalent basis by contrasting the reduced Raman spectrum I_{red}^p with the infrared derived quantities $\omega\epsilon_2$ and $\omega\text{Im}(-\epsilon^{-1})$, where p denotes *HH* or *HV* polarization and ϵ is the complex dielectric constant of the (isotropic) material.

The reduced Raman spectra are calculated from the direct spectra $I^p(\omega_L, \omega_S)$ (viz., Figs. 10–12) according to

$$I_{\text{red}}^p(\omega) \equiv I^p(\omega_L, \omega_S)(\omega_L + \Omega)^{-4} [n(\Omega)/\Omega]^{-1}, \quad (9)$$

where ω_L is the frequency of the incident (laser) light, and $\omega_S \equiv \omega_L + \Omega$ is the frequency of the scattered light. Thus, Ω is the Raman shift, and $\Omega < 0$ corresponds to the Stokes spectrum (creation of a phonon, as in Figs. 10–12) while $\Omega > 0$ gives the anti-Stokes spectrum (annihilation of a phonon, not shown), and $\omega \equiv |\Omega|$ is the phonon frequency. Here

$$n(\Omega) \equiv [\exp(\hbar\Omega/k_B T) - 1]^{-1} \quad (10)$$

is the Bose-Einstein occupation number for sample temperature T . For the Stokes spectrum, where $\Omega = -\omega < 0$, one has

$$n(\Omega)/\Omega = \omega^{-1} [n(\omega) + 1],$$

which is a more familiar form. For the anti-Stokes spectrum ($\Omega = \omega > 0$), one has $n(\Omega)/\Omega = \omega^{-1} n(\omega)$.

The real (ϵ_1) and imaginary (ϵ_2) parts of the complex dielectric constant $\epsilon (= \epsilon_1 + i\epsilon_2)$ can be computed from the reflectivity at normal incidence R using Kramers-Kronig techniques,⁶⁷ if R is measured over a sufficiently large frequency range. The expressions for doing this are as follows:

$$\varphi(\omega) \equiv \frac{1}{2\pi} \int_0^\infty \frac{d\ln R}{d\omega'} \ln \frac{\omega' + \omega}{\omega' - \omega} d\omega', \quad (11)$$

$$n = (1 - R)(1 + R - 2R^{1/2} \cos \varphi)^{-1}, \quad (12)$$

$$k = 2R^{1/2} \sin \varphi (1 + R - 2R^{1/2} \cos \varphi)^{-1}, \quad (13)$$

$$\epsilon_1 = n^2 - k^2, \quad (14)$$

$$\epsilon_2 = 2nk, \quad (15)$$

$$\text{Im}(-\epsilon^{-1}) = \epsilon_2(\epsilon_1^2 + \epsilon_2^2)^{-1}. \quad (16)$$

The results of applying these data-reduction procedures to Figs. 10–12 are shown in Figs. 13–15.

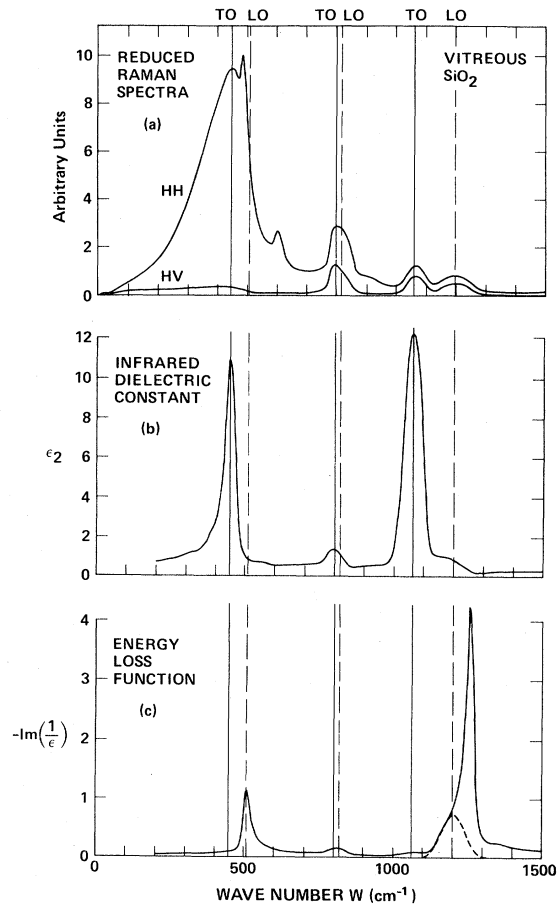


FIG. 13. Comparison of the reduced Raman spectra (a) of bulk *v*-SiO₂ with the imaginary parts of the infrared derived transverse (b) and longitudinal (c) dielectric functions. Peaks in $\epsilon_2 \equiv \text{Im}\epsilon$ and $\text{Im}(-\epsilon^{-1})$ mark transverse and longitudinal optical modes, respectively.

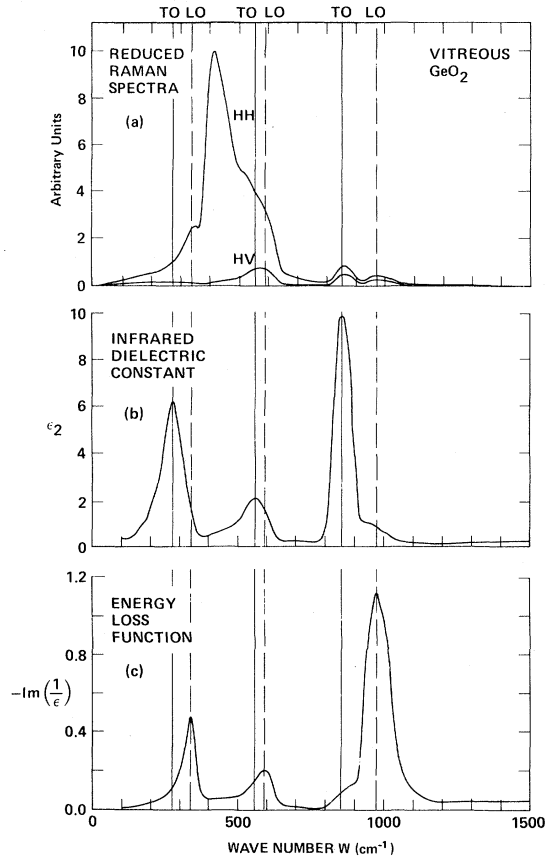


FIG. 14. Comparison of the reduced Raman spectra (a) of bulk ν - GeO_2 with the imaginary parts of the infrared derived transverse (b) and longitudinal (c) dielectric functions. Peaks in $\epsilon_2 \equiv \text{Im}\epsilon$ and $\text{Im}(-\epsilon^{-1})$ mark transverse and longitudinal optical modes, respectively.

There are no approximations in achieving the reduced Raman spectra (a), but there are two possible sources of error in ϵ_2 and $\text{Im}(-\epsilon^{-1})$. First is the truncation error, arising from the fact that reflectivity was not measured over the infinite range $0 \leq \omega \leq \infty$. Various reasonable extensions of the reflectivity data to lower ($< \sim 200 \text{ cm}^{-1}$) and higher ($> 1500 \text{ cm}^{-1}$) frequencies were tested and found to have very little effect on the frequencies of the main features in the derived ϵ_1 and ϵ_2 . This indicates that reflectivity was measured to frequencies that are sufficiently outside the range of the main resonances in ϵ_2 . A second possible source of error is the fact that reflectivity was not measured at normal incidence, for which Eqs. (11)–(13) hold, but at $\sim 20^\circ$ off normal. Substitution of off-normal data for R , although common, needs more investigation, and might account for the as yet unexplained “anomalous” sharp line in the high-frequency region of $\text{Im}(-\epsilon^{-1})$ for ν - SiO_2 [shown in Fig. 13(c), and previously commented on in Ref. 48].

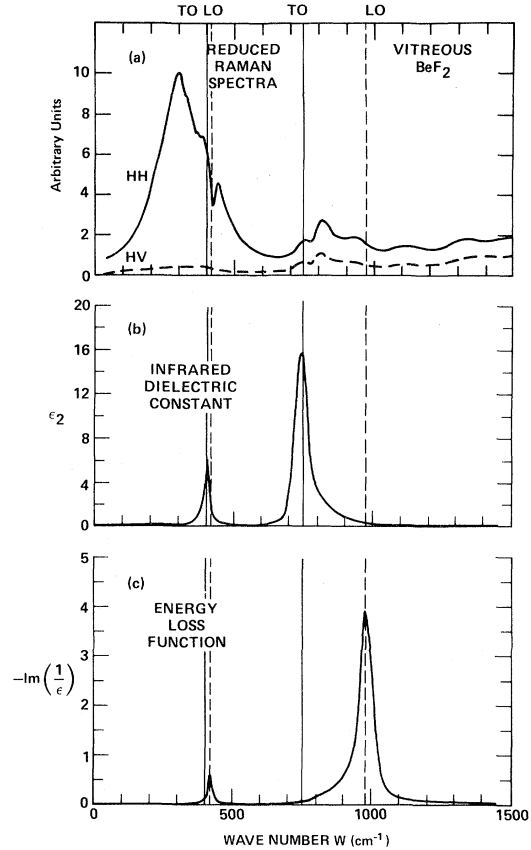


FIG. 15. Comparison of the reduced Raman spectra (a) of bulk ν - BeF_2 with the imaginary parts of the transverse (b) and longitudinal (c) dielectric functions. Peaks in $\epsilon_2 \equiv \text{Im}(-\epsilon^{-1})$ mark transverse and longitudinal optical modes, respectively.

E. Comparison of the reduced infrared and Raman response

Comparison of the ϵ_2 and $\text{Im}(-\epsilon^{-1})$ spectra reveals the presence of large transverse-optical–longitudinal-optical (TO-LO) splittings of the infrared response of these glasses.^{48–50} Peaks in ϵ_2 mark the frequencies of strong absorption of TO electromagnetic waves, for which the Maxwellian electric polarization \vec{P} is transverse to the propagation vector \vec{k} of the ir wave, i.e., $\vec{P} \perp \vec{k}$. Similarly, peaks in $\text{Im}(-\epsilon^{-1})$ mark the frequencies of strong absorption of LO waves (for which $\vec{P} \parallel \vec{k}$).

The data for ν - GeO_2 and ν - BeF_2 show that each TO peak in ϵ_2 has an associated LO peak in $\text{Im}(-\epsilon^{-1})$ at somewhat higher frequency, with comparable widths and similar strengths [relative to other lines in the ϵ_2 or $\text{Im}(-\epsilon^{-1})$ spectra]. With this in mind, Galeener and Lucovsky⁴⁸ have drawn the dashed curve in Fig. 13(c) as more representative of the true high-frequency LO response of ν - SiO_2 . The

odd-looking asymmetric sharp line actually computed from data is then assumed to be spurious, perhaps arising from treating the reflectivity data [Fig. 10(b)] as though it were taken at perfectly normal incidence, rather than 20° off normal.

Note that, in general, ϵ_2 contains weak peaks at positions of the strong peaks in $\text{Im}(-\epsilon^{-1})$ and vice versa. This is especially evident for the high-frequency TO-LO pairs in $\nu\text{-SiO}_2$ and $\nu\text{-GeO}_2$, Figs. 13 and 14. This may be a true effect, or it may be a result of treating the reflectivity as though it were taken at normal incidence. If the weak peaks are not artifacts, the existence of LO response (or weak lines of some other origin) in ϵ_2 and $\text{Im}(-\epsilon^{-1})$ should come out of a proper microscopic description of the infrared active modes involved. At the present level of understanding, the effect seems more likely to be spurious, indicating a need for new reflectivity measurements at angles closer to normal incidence, or for improved analysis of the present reflectivity curves.

Galeener and Lucovsky^{48,49} first noted that peaks corresponding to most of these TO-LO pairs appear in the Raman spectra of $\nu\text{-SiO}_2$ and $\nu\text{-GeO}_2$. Similar behavior has since been reported for $\nu\text{-BeF}_2$,⁵⁰ $\nu\text{-GeS}_2$,⁶⁸ $\nu\text{-As}_2\text{O}_3$,⁶⁹ $\nu\text{-As}_2\text{S}_3$,⁶⁹ $\nu\text{-As}_2\text{Se}_3$,⁶⁹ and $\nu\text{-B}_2\text{O}_3$.⁷⁰ There is also evidence for TO-LO splittings in heavy metal-halide glasses⁷¹ and $\nu\text{-P}_2\text{O}_5$.⁷²

These correspondences can be seen in Figs. 13–15 where the solid vertical lines mark the positions of peaks in ϵ_2 and the dashed lines mark peaks in $\text{Im}(-\epsilon^{-1})$. These lines are labeled TO and LO, respectively, at the top of the figures. One must consider all three figures to discern the following.

The high- and intermediate-frequency ir TO-LO pairs (above 600 cm^{-1} for $\nu\text{-BeF}_2$) correspond to relatively unpolarized peaks in the Raman spectra both in position and halfwidth. It is, therefore, reasonable to assign these Raman peaks to Raman activity of the corresponding infrared-active TO and LO modes. Proof of this assignment would require observation of some property of the Raman lines themselves that is indicative of TO and/or LO nature, such as near-forward polariton scattering.^{73–76} Such scattering requires observation of small shifts in frequency with changes in the scattering vector and is likely to be quite difficult, given the width of the lines. Since there also seems to be little reason to doubt the assignment, polariton scattering has not been attempted.

The situation appears to be more complex for the lowest-frequency TO-LO pair. These two lines occur in the wave-number range of the dominant Raman line which may obscure their observation in Raman spectra. The fact that the low-frequency TO peak occurs at the position of the dominant Raman

peak in $\nu\text{-SiO}_2$ is apparently an “accident,” since this coincidence does not appear in $\nu\text{-GeO}_2$ or $\nu\text{-BeF}_2$. The fact that the low-frequency LO mode aligns with a (subsidiary) peak in the Raman spectrum of $\nu\text{-GeO}_2$ also appears to be an accident, since this coincidence does not appear to occur in $\nu\text{-SiO}_2$ or $\nu\text{-BeF}_2$. Also, the lowest-frequency TO and LO lines in ϵ_2 and $\text{Im}(-\epsilon^{-1})$ are much narrower than the structures seen in the same frequency region of the Raman spectra. In short, these lowest-frequency TO-LO pairs appear to be Raman inactive.

This conclusion contradicts an earlier tentative assignment⁴⁸ of the sharp 495-cm^{-1} Raman line as an LO mode in $\nu\text{-SiO}_2$, but is consistent with a more recent attribution to symmetric stretch motions of nearly planar fourfold Si-O rings.^{77,78} The latter work⁷⁸ also assigns the 606-cm^{-1} Raman line to planar threefold rings in $\nu\text{-SiO}_2$. Numerous other models have been proposed for these small sharp highly polarized lines,^{79–87} but their origin will not be further discussed in this paper.

IV. THEORETICAL PRELIMINARIES

A. Historical background

Before describing the comparison between neutron, Raman, and ir spectra, it is useful to establish a simple theoretical picture to guide interpretation of our observations. Historically, several methods have been used in attempts to understand the vibrational properties of tetrahedral glasses, most of them centered on understanding $\nu\text{-SiO}_2$. The earliest method seems to have been to compare spectral features with calculated frequencies of an isolated tetrahedral “molecule,” e.g., SiO_4 . Larger molecular units were considered in an attempt to account for the fact that the SiO_4 “units” are not isolated in the glass, but actually share the oxygen atoms at their corners. Wadia and Bolloomal⁸⁸ used an anchored tetrahedron model, in which the oxygen atoms of the SiO_4 unit were each connected to another atom A of infinite mass, with the Si—O— A angle set at 180° . Lucovsky and Martin⁸⁹ have suggested that intertetrahedral coupling be accounted for by considering the vibrations of two molecular units, here the SiO_4 tetrahedron and the Si—O—Si waterlike molecule. All these methods have proven to be seriously inadequate because they do not properly account for the “coupling” of the SiO_4 tetrahedral units.

The intertetrahedral coupling is more adequately accounted for in three more recent developments, the large-cluster calculations of Bell and Dean^{12–21} (BD), the central-force network model of Sen and Thorpe^{26–28} (ST), and the cluster Bethe-lattice cal-

culations of Laughlin and Joannopoulos⁹⁰⁻⁹² (LJ). The most complete of these methods (in that it includes quantitative disorder) is the BD calculation, some results of which have already been used in this paper. While the BD method is of great heuristic value and promising accuracy, it is cumbersome to employ since a definite set of coordinates for a large piece of the glass structure must be established and treated by large capacity computing methods. Much useful information has also been obtained using the elegant methods of LJ; however, these procedures also require the development of sophisticated theoretical methods and computer routines for application to materials other than the $v\text{-SiO}_2$ already treated. The BD and LJ methods include both bond-stretching (central-) force constants α and bond-bending (non-central-) force constants, which we collectively call β in this paper.

B. Central-force network dynamics

The central-force calculation of ST is unique in that it arrives at simple analytical results, at the expense of excluding noncentral forces (β) from consideration. Galeener³⁴ has made a quantitative study of the accuracy of the ST results and shown that for $v\text{-SiO}_2$, $v\text{-GeO}_2$, and $v\text{-BeF}_2$, the center frequencies of the intermediate- and high-frequency bands of these glasses (ω_3 and ω_4 in ST) are calculated within 5% of the values given by the BD large-cluster calculation. This remarkable accuracy, coupled with the simplicity of application, has encouraged us to use the ST central-force model as a basis for discussion of our comparison of neutron, Raman, and ir spectra.

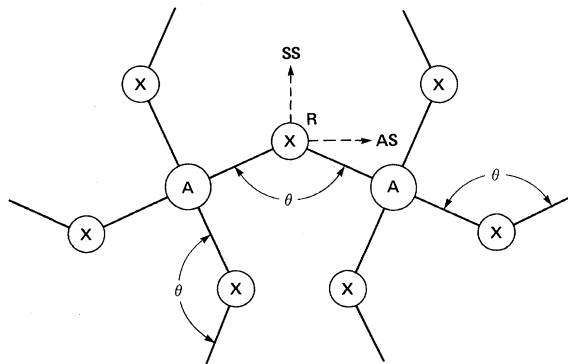


FIG. 16. Schematic diagram of the local order assumed in the central-force-only continuous-network model for an AX_2 glass. Note the common intertetrahedral angle θ . The X -atom motions shown are defined as symmetric stretch (SS), antisymmetric stretch (AS), and rocking (R).

A detailed application of the central-force model to the Raman and ir spectra of the present materials has been presented elsewhere.³⁴ Those aspects relevant to the present discussion will be related with the help of Fig. 16. This figure shows schematically the three-dimensional local order assumed for an AX_2 tetrahedral glass, such as the glasses considered in this paper. This local topology is repeated throughout space in the model: all $A-X$ bond distances are the same, all $X-A-X$ angles have the tetrahedral value $\cos^{-1}(-\frac{1}{3}) \approx 109.5^\circ$, and all intertetrahedral (bridge) angles $A-X-A$ have the common value θ . The ring statistics of the structure are unspecified.⁹³ The dihedral angles (δ) giving the orientation of two neighboring tetrahedra relative to the $A-X-A$ plane are also unspecified, and this allows for disorder in the system. If the dihedral angles are not ordered, the system is not periodic and may have any kind of ring statistics, including no rings (the Bethe lattice⁹⁴). The dashed arrows in Fig. 16 indicate those motions of the X atoms which turn out to be canonical, where SS stands for symmetric stretch, AS for antisymmetric stretch, and R for rocking motion.

ST assumed that all force constants in this structure were zero except for the $A-X$ bond-stretching constant α . The only simple analytical results obtained were for the spectral limits ω_i ($i=1,2,3,4$) of the two highest-frequency bands in the density of vibrational states of such a system. Formulas for these are given later in this paper [Eqs. (24)-(27)]. These band-edge limits are plotted versus $\cos\theta$ as the solid straight lines in Fig. 17. The vibrational density of states for the model is indicated schematically by the dashed lines in Fig. 17 for two different angles θ . The relative weights in the VDOS are given in parentheses, with vertical arrows indicating δ functions of unit area. These states account for four of the nine expected per formula unit AX_2 ; the oth-

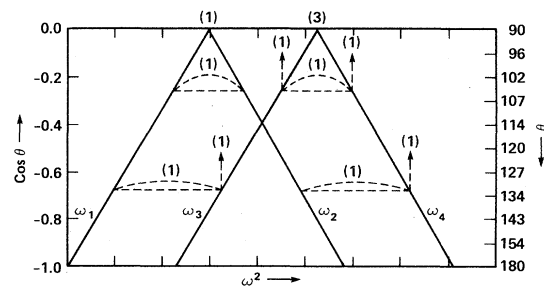


FIG. 17. Diagram of the band-edge limits for the central-force-only model [Eqs. (24)-(27)], showing dependence on θ . The dashed lines are a schematic representation of the density of vibrational states at two different values of θ , with relative weights given in parentheses.

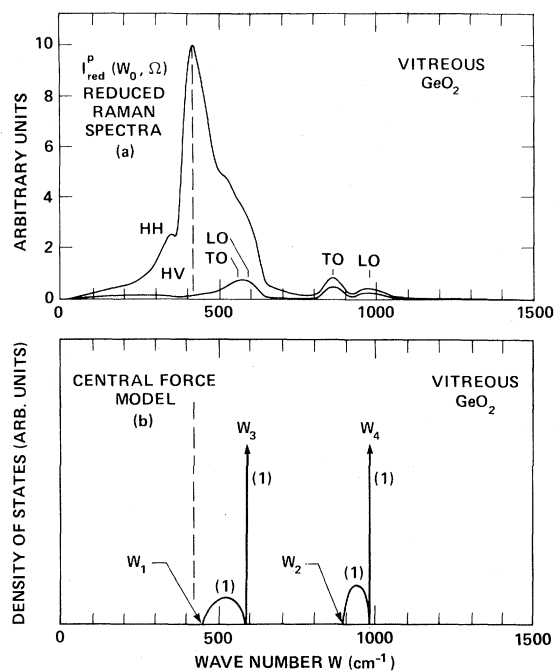


FIG. 18. Fitting of W_3 and W_4 in the central-force-only model (b) to the LO modes in the Raman spectra (a) of v - GeO_2 . Note that the lowest-frequency band limit W_1 is predicted to be near the position of the dominant peak in the Raman spectrum.

ers are driven to zero frequency by their acoustic nature, and by the assumption that the non-central-force constant β is zero.

Application of these band-edge limits to interpretation of ir and Raman spectra depends on proper treatment of the TO-LO splittings. Since the ST theory (and all others mentioned in Sec. IV A) does not include the long-range electromagnetic forces leading to TO-LO splittings, it can predict only one mode for each confirmed TO-LO pair. It has been argued elsewhere⁴⁸⁻⁵⁰ that this "bare mode," whose frequency is split by Coulomb interactions, lies nearer the LO than the TO frequency. Thus the frequencies of the δ functions, ω_3 and ω_4 , are identified provisionally with the experimental values of the intermediate- and high-frequency LO modes, respectively. This enables calculation of α , θ , and the other two band limits ω_1 and ω_2 . A detailed discussion for v - SiO_2 , v - GeO_2 , and v - BeF_2 can be found in Ref. 34.

One result of this procedure is illustrated in Fig. 18, for v - GeO_2 . Having fit ω_3 and ω_4 to the LO peaks, note that the band limit ω_1 is predicted to be very close to the position of the dominant Raman peak (marked by the dashed vertical line). A similar correspondence was found for all three AX_2 glasses,

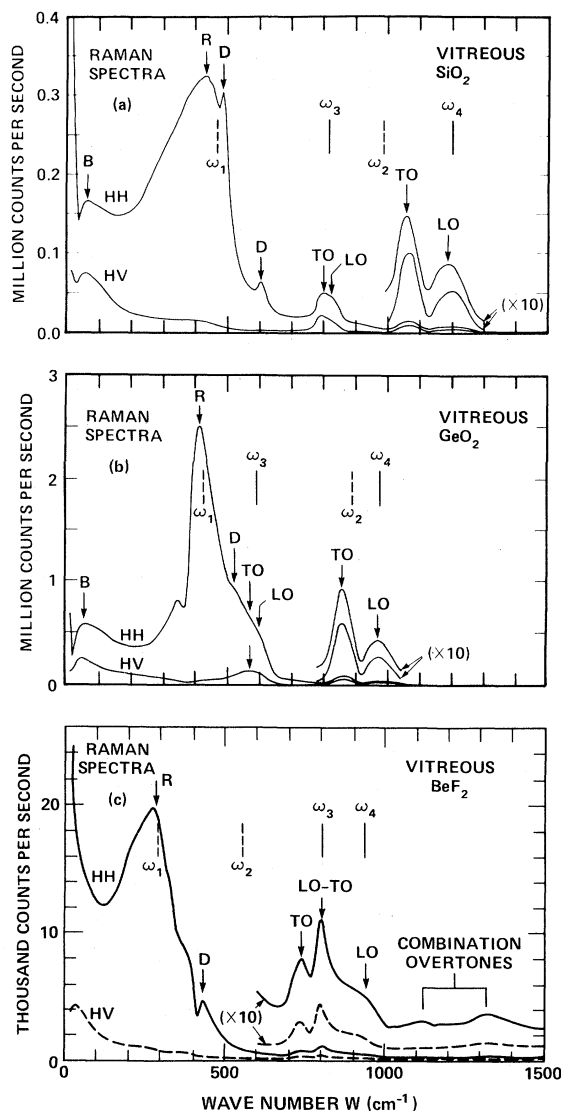


FIG. 19. Fit of the central-force-only model [Eqs. (24)–(27)] to the Raman spectra of (a) v - SiO_2 , (b) v - GeO_2 , and (c) v - BeF_2 . The solid vertical lines mark empirical (LO) values of the frequencies W_3 and W_4 which are input to the analysis, while the dashed vertical lines are subsequent predictions of W_1 and W_2 . It is found that W_1 always lies near the dominant highly polarized Raman line R, while W_2 does not correspond consistently to any spectral feature. W_1 is found in the theory to correspond to pure SS motion (as defined in Fig. 16) while W_2 corresponds to pure AS motion, with the cations (A atoms in Fig. 16) at rest in both cases.

as shown in Fig. 19, where the solid vertical lines represent frequencies input to the analysis and dashed vertical lines represent output. While ω_1 is always near the dominant Raman peak (R), ω_2 does not consistently correspond to any spectral feature, and these selection rule observations are now under-

stood^{35,95} as follows.

The state at ω_1 in the ST model is unique. It involves in-phase SS motion of all the X atoms in the glass while the A atoms are perfectly at rest, and this is said³⁴ to be the approximate character of the mode responsible for the dominant Raman line R in each glass. This assignment has been supported by several results, including observation⁹⁶ of isotopic shifts for $^{16}\text{O} \rightarrow ^{18}\text{O}$ in $\nu\text{-SiO}_2$ that are consistent with no Si motion in R . It has also been shown by "graphical construction"⁹⁵ that pure SS motion (as at ω_1) should be Raman active, while pure AS motion (as at ω_2) should be Raman inactive. Using a Wolkenstein bond-polarizability model,⁹⁷ Martin and Galeener³⁵ have shown that there is a δ function in the coupling coefficient for the "polarized portion" of Raman scattering at ω_1 in the ST model. Thus R in Fig. 19 is assigned to very strong Raman activity by a relatively small number of states having SS motion, and should, therefore, not normally correspond to a peak in the VDOS.

The "polarized portion" (PP) of the Raman response is given by a simple linear combination of the HH and HV spectra:

$$I^{\text{PP}}(\omega) = I^{\text{HH}}(\omega) - \frac{4}{3} I^{\text{HV}}(\omega). \quad (17)$$

For a collection of randomly oriented and isolated identical scatterers (like molecules in a gas or liquid), this quantity is known⁶³ to involve only the diagonal elements of the Raman tensor of each molecule, while the HV spectrum involves only the off-diagonal elements. Martin and Galeener³⁵ have shown that these properties hold for the bond-polarizability tensor treatment of an AX_2 glass in central forces only. Thus we may regard the directly measured HH spectrum as a linear combination of the more fundamental HV and PP spectra.

V. INTERCOMPARISON OF NEUTRON, RAMAN, AND INFRARED SPECTRA

A. Reduced spectra

As mentioned earlier, Galeener and Sen³³ (GS) have shown that Raman and ir spectra of disordered solids can be compared on an equivalent basis by contrasting the reduced Raman spectrum I_{red}^p with the infrared quantities $\omega\epsilon_2$ and $\omega \text{Im}(-\epsilon^{-1})$, whose extraction from experiment is described in Sec. III D. In particular, GS found that

$$I_{\text{red}}^p(\omega) \sim \sum_b C_b^p(\omega_L, \omega) \rho_b(\omega), \quad (18)$$

$$\omega\epsilon_2 \sim \sum_b D_b(\omega) \rho_b(\omega), \quad (19)$$

$$\omega \text{Im}(-\epsilon^{-1}) \sim \sum_b D_b'(\omega) \rho_b(\omega), \quad (20)$$

where the coupling coefficients C_b , D_b , D_b' all derive their frequency dependence from that of the eigenvector amplitudes in expressions of the form

$$D_b(\omega) = \sum_I M_I |U_I^b(\omega)|^2.$$

Here b represents a "band" of states, \sum involves a sum over three orthogonal directions at each of all sites, I , M_I is a quantity independent of phonon frequency, and $U_I^b(\omega)$ is the frequency-dependent amplitude of the eigenvector indicated by I and b . In general, these coupling coefficients D_b , etc., are unknown and may vary rapidly over a band,³³ as has been shown to be the case for the dominant Raman line (in Sec. IV B and Refs. 34 and 35).

The coupling coefficients (or matrix elements) in Eqs. (18)–(20) could be determined experimentally, apart from a multiplicative constant, if the subband densities of states $\rho_b(\omega)$ could be measured directly. No method for doing the latter is yet known, and indeed the precise meaning of a subband is not easy to define in an experiment. A substitute procedure is to compare the optical spectra against the total VDOS,

$$\rho(\omega) = \sum_b \rho_b(\omega),$$

which can be estimated from inelastic neutron scattering. It was argued by Leadbetter and Stringfellow³⁹ that, for inelastic neutron scattering from $\nu\text{-SiO}_2$,

$$G^1(Q, \omega) \sim A(Q, \omega) \rho(\omega), \quad (21)$$

where the coefficient A is a slowly varying function of ω over the entire one-phonon frequency range (with the possible exception of low frequencies). The direct experimental function $G(Q, \omega)$ is determined from the differential scattering cross section by Eq. (6) and is shown in Fig. 4 for all three materials. $G^1(Q, \omega)$ indicates the one-phonon contribution, obtained by subtracting an estimate of the multiphonon contributions (also shown in Fig. 4). The resultant $G^1(Q, \omega)$ were shown in the upper panels of Figs. 5–7. Since the estimates of multiphonon contribution in Fig. 4 are approximate, and are themselves slowly varying functions of ω , we shall merely keep them in mind and make our comparisons with the *uncorrected* quantities $G(Q, \omega)$.

The reduced Raman spectra and infrared $\omega\epsilon_2$ are compared with the neutron estimate of the VDOS $G(Q, \omega)$, in Figs. 20–22. The longitudinal response $\omega \text{Im}(-\epsilon^{-1})$ is not shown, for simplicity; its main features appear at the positions marked LO in the Raman spectra and can be seen directly in Figs. 13–15. The vertical line at TO marks the peaks in $\omega\epsilon_2$, D the sharp "defect" lines in the HH

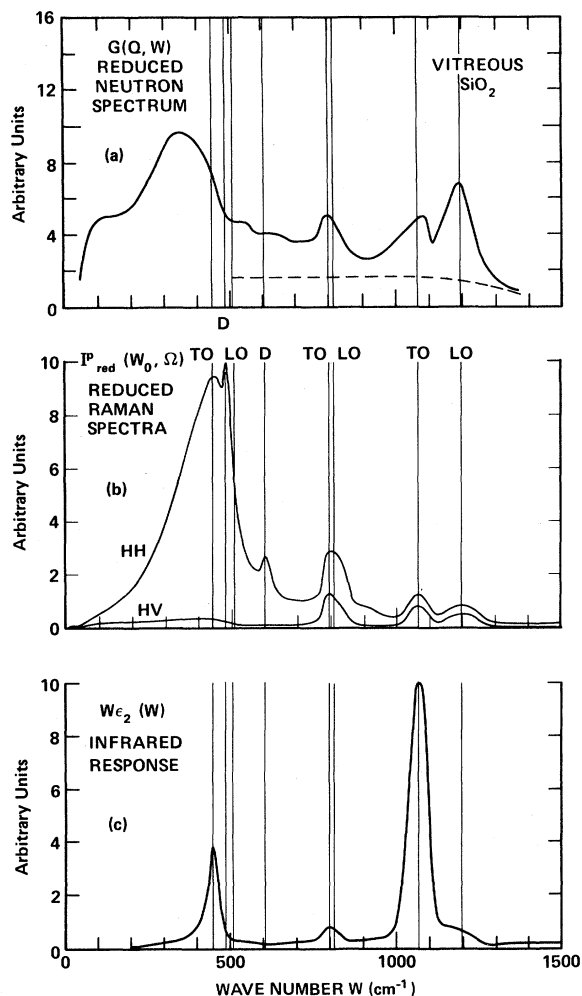


FIG. 20. Comparison of the Raman (b) and infrared (c) bands of ν - SiO_2 with the inelastic neutron scattering estimate of the vibrational density of states approximated by $G(Q, W)$ in (a). Note especially the splitting of the high-frequency bands of $G(Q, W)$ into a TO-LO pair, and the fact that the HV Raman spectrum mimics [cf. Eq. (22)] the density of states, while the HH spectrum does not.

Raman spectrum, and R the position of the dominant (HH) Raman line. The curves for $G(Q, \omega)$ are taken from Fig. 4, where the uncertainty can be judged. The resolution in the neutron data varies with ω , and can be approximated by 0.05ω ; the resolution is better than 5 cm^{-1} in the Raman and ir data.

B. Empirical selection rules

Note first in Figs. 20–22 that the high-frequency lines identified as TO-LO pairs in Sec. III E correspond to separate peaks in $G(Q, \omega)$. Thus these opti-

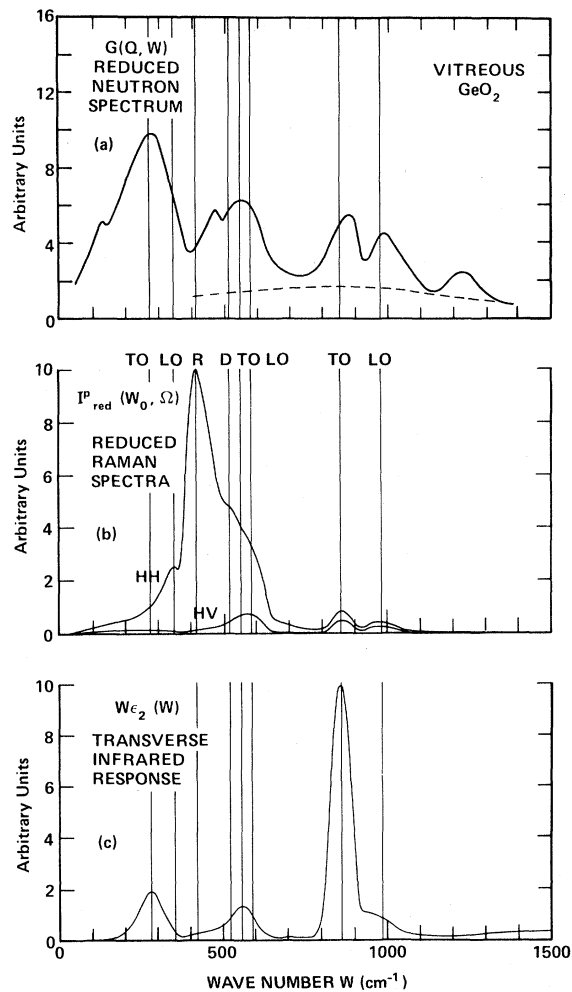


FIG. 21. Comparison of the Raman (b) and infrared (c) bands of ν - GeO_2 with the inelastic neutron scattering estimate of the vibrational density of states approximated by $G(Q, W)$ in (a). Note again the splitting of the high-frequency bands of $G(Q, W)$ into a TO-LO pair, and the fact that the HV Raman spectrum mimics [cf. Eq. (22)] the density of states, while the HH spectrum does not. Also note that the dominant Raman line R in the HH spectrum clearly lies near the low-frequency edge of a band of states, as predicted by the central-force model illustrated in Fig. 18.

cal features are associated with separate peaks in the $VDOS$, and their existence in the Raman spectra should not be ascribed to variation of matrix elements over a single band in the $VDOS$. These neutron scattering bands are well separated in ν - SiO_2 and ν - GeO_2 , where widths $\sim 50 \text{ cm}^{-1}$ larger than in the optical spectra have been observed, in accordance with the poorer neutron scattering resolution in ω .

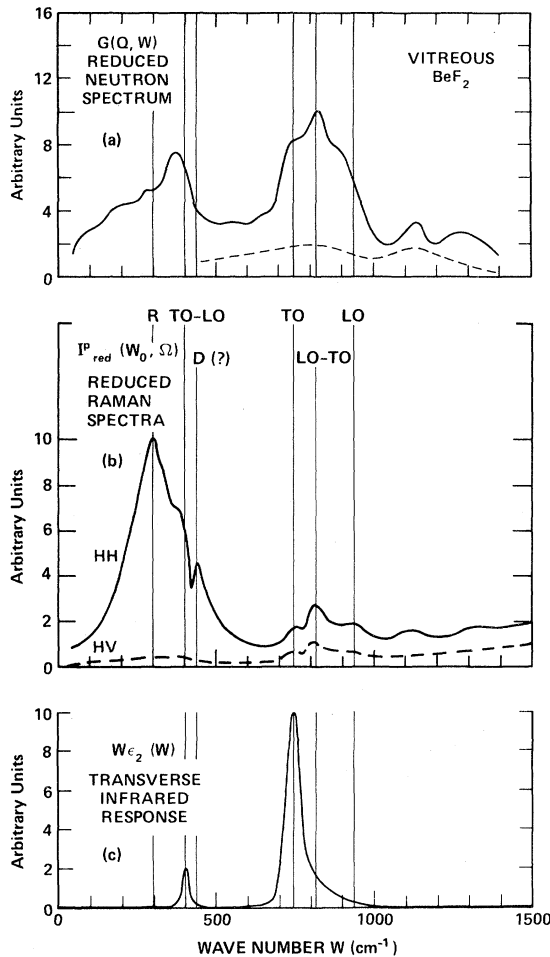


FIG. 22. Comparison of the Raman (b) and infrared (c) bands of v -BeF₂ with the inelastic neutron scattering estimate of the vibrational density of states approximated by $G(Q, W)$ in (a). Note the splitting of the high-frequency bands of $G(Q, W)$ into TO-LO pairs, and the fact that the HV Raman spectrum mimics [cf. Eq. (22)] the density of states while the HH spectrum does not.

The apparent equality of linewidths suggests that, in this frequency regime, the optical spectra I_{red}^p and $\omega\epsilon_2$ have strength S given approximately by

$$S(\omega) = \sum_b C_b \rho_b(\omega). \quad (22)$$

That is, the spectra can be represented approximately as a linear combination of the subband densities of states $\rho_b(\omega)$ with a different frequency-independent coefficient C_b applying over the width of each band b . In such cases, we say that the spectrum mimics the VDOS. The optical spectra then trace out the shapes of the vibrational subbands.

The intermediate-frequency TO-LO pairs in Raman and ir also appear to mimic the VDOS. This

can be seen in Figs. 20–22 in the vicinity of ~ 800 cm^{-1} for v -SiO₂, ~ 550 cm^{-1} for v -GeO₂ (except for HH spectrum), and 700 – 1000 cm^{-1} for v -BeF₂. The peaks in $G(Q, \omega)$ above 1150 cm^{-1} for v -GeO₂ and 1000 cm^{-1} for v -BeF₂ appear to be a two-phonon response, although the signal-to-noise ratio is quite poor in this region (cf. Figs. 1–4).

In the low-frequency region of Figs. 20–22, the HH Raman spectra, $\omega\epsilon_2$ and $\omega \text{Im}(-\epsilon^{-1})$ do not seem to mimic the VDOS. This can be seen at $\omega < 500$ cm^{-1} in all three glasses. In general, the low-frequency peak in $\omega\epsilon_2$ is much narrower than the structures of $G(Q, \omega)$ in the region $\omega < 500$ cm^{-1} . Although the peaks in $\omega\epsilon_2$ and $G(Q, \omega)$ align at ~ 280 cm^{-1} in v -GeO₂, similar coincidences are not seen in v -SiO₂ and v -BeF₂. No obvious pattern emerges, and we are unable to postulate “selection rules” for infrared activity of modes in this region of the spectrum. Theoretical progress in this problem is likely to depend on inclusion of noncentral forces, as will be discussed in Sec. VI.

On the other hand, the reduced HV Raman spectrum mimics the VDOS in all three glasses, showing bands of similar width and peak frequency as seen in $G(Q, \omega)$ for all values of ω . This remarkable correspondence has been supported, although not proven, by bond-polarizability calculations.^{35,95} The correspondence is potentially quite useful, since obtaining the HV Raman spectrum of most amorphous materials is easier and accessible to more experimentalists than is the acquisition of $G(Q, \omega)$ from neutron scattering.

Finally, we turn to comparison of the reduced HH Raman spectrum with $G(Q, \omega)$. The HH spectrum mimics the VDOS in the intermediate- and high-frequency regions, presumably because it contains an intrinsic admixture of the HV spectrum [as discussed in connection with Eq. (17)]. For frequencies up through the dominant Raman line R , the HH spectrum clearly does *mimic* $G(Q, \omega)$. As discussed in Sec. IV B, this is because of strong matrix-element effects favoring SS motions in the polarized portion of the response I_{red}^{pp} .

An example of the polarized portion of the Raman spectrum is shown in Fig. 23 for v -GeO₂; it was calculated from the experimental spectra in Fig. 21(b) using Eq. (17). As in the other two glasses, this spectrum is qualitatively the same as the directly measured HH spectrum for frequencies up through the dominant Raman line R , since $I_{red}^{HV} \ll I_{red}^{HH}$ in this region. Note that R occurs near a minimum in $G(Q, \omega)$, which we interpret as being near the low-frequency edge of the band of states that peaks near 500 cm^{-1} in $G(Q, \omega)$; this is just as predicted by the central-force model discussed in Sec. IV B, and illustrated in Fig. 18.

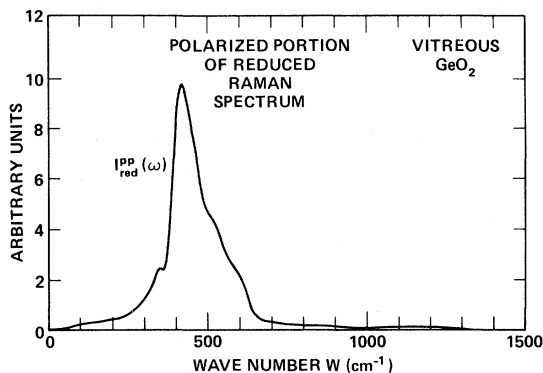


FIG. 23. Polarized portion (PP) of the reduced Raman spectrum of ν -GeO₂, obtained from Fig. 21(b) by subtracting $\frac{4}{3}$ of the HV spectrum from the HH spectrum, according to Eq. (17). Note the absence of the higher-frequency bands and that this PP spectrum does not mimic any feature in the density of states shown in Fig. 21(a).

Also note that R in ν -SiO₂ and ν -BeF₂ does *not* occur at a maximum in $G(Q, \omega)$, and may also be interpreted as occurring near the low-frequency edge of a subband of states. However, the latter interpretation is less straightforward than was the case for ν -GeO₂. For example, there is no convincing peak in $G(Q, \omega)$ for ν -SiO₂ in the region immediately above R (i.e., 450–750 cm⁻¹). Also, R in ν -BeF₂ is below the position of the lowest-frequency peak in $G(Q, \omega)$, rather than above it (as is the case in ν -SiO₂ and ν -GeO₂). In the following section, we interpret this reversal as indicating a rather large value of β/α for ν -BeF₂, as was first suggested in Ref. 34.

VI. AN AUGMENTED CENTRAL-FORCE ANALYSIS

A. The frequencies and force constants

In Ref. 34, Galeener has shown that peaks in the theoretical VDOS of the large-cluster calculation by

Bell, Dean, and Hibbins-Butler¹⁶ (BDH) can be predicted within $\sim 5\%$ by evaluating ω_0 , ω_3 , and ω_4 from the following expressions:

$$\omega_0^2 = 2\beta/m_X, \quad (23)$$

$$\omega_1^2 = (\alpha/m_X)(1 + \cos\theta), \quad (24)$$

$$\omega_2^2 = (\alpha/m_X)(1 - \cos\theta), \quad (25)$$

$$\omega_3^2 = (\alpha/m_X)(1 + \cos\theta) + (4\alpha/3m_A), \quad (26)$$

$$\omega_4^2 = (\alpha/m_X)(1 - \cos\theta) + (4\alpha/3m_A), \quad (27)$$

where θ is taken as the most probable value of the $A-X-A$ angle, m_X and m_A are the masses of the X and A atoms, and α and β are the central and non-central-Born-force constants, respectively. From Table I of Ref. 34, it can be verified that these expressions allow quite accurate deduction of β/α from the BDH data. Errors in β/α are typically $\sim 5\%$.

The frequency ω_0 was tentatively identified with pure rocking motion of the X atom (out of the plane of Fig. 16) accompanied by little or no motion of the A atoms.³⁴ Equation (23) was first derived for transverse motion of X atoms in the case of straight bonds ($\theta = 180^\circ$) by Kulas and Thorpe²⁷ and involves only the non-central-force constant β , since no bonds are stretched in this motion. Equations (24)–(27) are the band-limit formulas for central forces only, first derived by Sen and Thorpe,²⁶ and applied to interpret the dominant Raman line $R = \omega_1$ by Galeener.³⁴ This latter interpretation is outlined in Sec. IV (B) and is unchanged by our comparison of the Raman spectra with $G(Q, \omega)$.

In Table III of Ref. 34, experimental values of θ and α were deduced, using Eqs. (24) and (26) in order to minimize uncertainty due to the large TO-LO splitting of ω_4 , while β was taken from Eq. (23). That is,

$$\alpha = (\omega_3^2 - \omega_1^2)(3m_A/4), \quad (28)$$

$$\cos\theta + 1 = \omega_1^2(\omega_3^2 - \omega_1^2)^{-1}(4m_X/3m_A), \quad (29)$$

TABLE II. An application of the augmented central-force model to the experimentally determined wave-number values W_0 , W_1 , and W_3 , using Eqs. (23)–(30). Here W_0 is taken from neutron data, while $W_1 (= W_R)$ and W_3 are taken from the HH Raman spectra, as given in Figs. 20–22. W is in units of cm⁻¹, α , and β in N/m. The resultant neutron values for β/α differ significantly from that (0.18) used by Bell, Dean, and Hibbins-Butler (Ref. 16) in their large-cluster calculations for all three materials, and differ somewhat from infrared values, deduced by Galeener (Ref. 34) using infrared estimates of W_0 .

AX_2	W_R	W_3	θ (deg)	α	W_4	W_0	β	β/α
SiO ₂	450	800	130	545	1176	350	58	0.11
GeO ₂	420	556	128	431	930	290	40	0.09
BeF ₂	295	810	125	228	941	370	77	0.34

$$\beta = \frac{1}{2} \omega_0^2 m_X. \quad (30)$$

In evaluating these, ω_3 and $\omega_1 = \omega_R$ were taken from the Raman data, and the present study provides no reason to change the results for α and θ , which are presented in Table II.

On the other hand, the value of ω_0 was identified with the low-frequency peak in $\omega\epsilon_2$. Since we have just shown that this ir peak does not always correspond accurately to a peak in $G(Q, \omega)$, it now appears better to associate ω_0 with the low-frequency peak in the neutron determined $G(Q, \omega)$. The latter is expected to be a better approximation to the VDOS in this region of the spectra. The modified results are given in Table II of this paper, where the values of ω_0 were taken from the low-frequency peaks of $G(Q, \omega)$ in Figs. 20–22. This produces new estimates of β and β/α , but the values of $\omega_R = \omega_1$, ω_3 , θ , α , and ω_4 remain as first given and discussed in Ref. 34. The last column in Table II, based on the neutron estimate for β , indicates that the value of $\beta/\alpha = 0.18$ used¹⁶ by BDH was rather large for ν -SiO₂ and ν -GeO₂, and rather small for ν -BeF₂. Since the discrepancies are large (approximately twofold), it would be interesting to repeat the BDH calculations using values of β/α more like those given in Table II.

B. The idealized densities of states

Inclusion of the rocking motion modeled by Eq. (23) adds one degree of freedom for each X atom. (The other two degrees of freedom of the X atom in the Si-O-Si plane of Fig. 16 are already accounted for by the central-force-only model.) This means that ω_0 adds two vibrational modes to the VDOS per formula unit AX_2 . The total count per formula unit at this point is four modes for central forces only [cf. Fig. 18(b)], plus two modes for rocking motion of the X atoms, leaving three modes per formula unit not explicitly accounted for. We assign these three modes to the three degrees of freedom of the center of mass motion of a formula unit, i.e., essentially to acoustic modes of the glass, which in the present approximation would have virtually zero frequency.

We have thus arrived at a simplified model based on nearest-neighbor central forces only, augmented by rocking motions and acoustic modes associated with approximate inclusion of nearest-neighbor non-central Born forces ($\beta \neq 0$). This highly idealized augmented central-force model gives a schematic VDOS for the three glasses, as shown by the solid lines and δ functions (vertical arrows) in Figs. 24–26. The frequencies ω_0 through ω_4 in these fig-

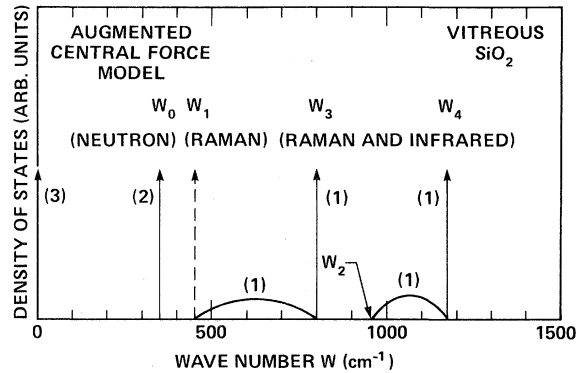


FIG. 24. Schematic diagram of the vibrational density of states of ν -SiO₂ according to the augmented central-force model. Two rocking modes are placed at W_0 , the position of the low-frequency peak in the neutron data of Fig. 20(a). Three acoustic modes are placed at $W \approx 0$. These five modes augment the four units of states already predicted by central forces only. The dashed vertical arrow marks the expected position of the dominant Raman line, at W_1 .

ures are as deduced earlier and listed in Table II. The singularity in the Raman matrix element for polarized Raman scattering is marked by the dashed δ function at ω_1 , as discussed in Sec. IV B.

In reality, these bands and δ functions are spread by disorder in the glass structure and by the neglected effects of the mode couplings that must occur when both central and noncentral forces are included simultaneously. The acoustic modes are spread to frequencies above $\omega = 0$, as in a Debye model.

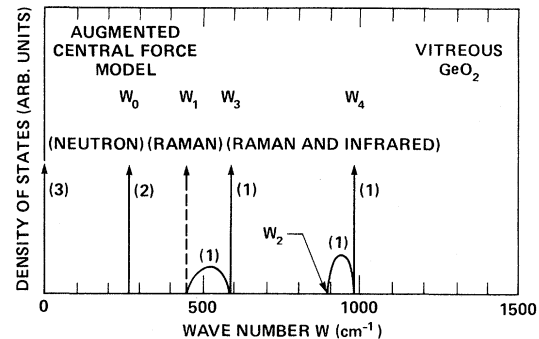


FIG. 25. Schematic diagram of the vibrational density of states for ν -GeO₂ according to the augmented central-force model. The two rocking modes at W_0 and three acoustic modes at $W \approx 0$ are in addition to the four units of states predicted by the central-force-only model, shown in Fig. 18(b). The dashed vertical arrow marks W_1 , the expected position of the dominant Raman line.

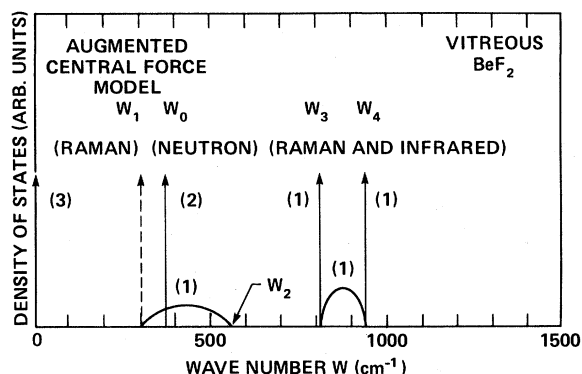


FIG. 26. Schematic diagram of the vibrational density of states for ν -BeF₂ according to the augmented central-force model. In this case, neutron data reveal that the two rocking modes occur at a wave-number value (W_0) greater than that of the dominant Raman line (W_1), hence they overlap the $W_1 \rightarrow W_2$ band, and strong mode interactions may occur.

C. An empirical study of the subband densities of states

The augmented central-force (ACF) model nevertheless allows prediction of the relative weights of bands in appropriate frequency regions of the VDOS. For ν -SiO₂, Fig. 24 reveals that $\frac{2}{9}$ of the states should appear between ~ 900 and ~ 1300 cm⁻¹, allowing for broadening due to disorder and mode coupling. Another $\frac{2}{9}$ should appear between

~ 450 cm⁻¹ and ~ 900 cm⁻¹. These $\frac{4}{9}$ of the states exist in central forces only; inclusion of noncentral forces perturbs their frequencies without changing their number. The ACF model predicts another $\frac{2}{9}$ of the states to be spread around the rocking frequency ω_0 , whose position is ~ 350 cm⁻¹ when taken from the neutron data as in Table II. The remaining $\frac{3}{9}$ are acoustic modes (shown at zero frequency in Fig. 24, but expected to lie between 0 cm⁻¹ and some effective Debye frequency). The expectations for ν -GeO₂ are qualitatively similar as can be deduced from Fig. 25. On the other hand, Fig. 26 shows that the weights group differently in ν -BeF₂, with $\frac{3}{9}$ of the states from ~ 700 to ~ 1000 cm⁻¹, $\frac{3}{9}$ from ~ 250 to ~ 700 cm⁻¹, and $\frac{3}{9}$ below ~ 250 cm⁻¹.

These predictions compare rather well with the VDOS calculated for a large cluster by Bell and Dean,¹⁸ shown in Figs. 5(b), 6(b), and 7(b). We have integrated the area under the large-cluster $\rho(\omega)$ curves in those figures and determined the frequencies marking $\frac{3}{9}$, $\frac{5}{9}$, etc. of the total area, as given in the $\rho(\omega)$ column of Table III. These frequencies divide the spectra into groups which are shown in Fig. 27 and correspond approximately to bands anticipated from the ACF model. The division is not expected to be perfect since the $\rho(\omega)$ in Fig. 27 are for the case of a cluster all of whose surface atoms X are fixed in place. Such a cluster is not stoichiometrically AX₂, and the fixing of surface

TABLE III. Division of the density-of-states data into bands having relative weights as predicted by the augmented central-force model. Here $\rho(\omega)$ is the theoretical VDOS calculated by Bell and Dean (Ref. 18) for a large-cluster model with fixed atoms on its surface. $G^1(Q, \omega)$ is the experimental quantity related to the (one-phonon) vibrational density of states and reported in Figs. 5–7 of this paper. The wave-number ranges listed here for $\rho(\omega)$ are shown graphically in Fig. 27, while those for the experimental $G^1(Q, \omega)$ are shown in Fig. 28.

Glass	Augmented central-force modes	Integrated fraction of states $\times 9$	Wave-number range (cm ⁻¹)	
			Large cluster $\rho(\omega)$	Neutron scattering $G^1(Q, \omega)$
SiO ₂	Acoustic	3.0	0 – 380	0 – 330
	Rocking	2.0	380 – 500	330 – 480
	$W_1 \rightarrow W_3$ bands	2.0	500 – 800	480 – 900
	$W_2 \rightarrow W_4$ bands	2.0	800 – 1120	900 – 1350
GeO ₂	Acoustic	3.0	0 – 320	0 – 260
	Rocking	2.0	320 – 420	260 – 430
	$W_1 \rightarrow W_3$ bands	2.0	420 – 590	430 – 660
	$W_2 \rightarrow W_4$ bands	2.0	590 – 950	660 – 1100
BeF ₂	Acoustic	3.0	0 – 190	0 – 400
	Rocking	2.0	190 – 260	400 – 700
	$W_1 \rightarrow W_2$ bands	1.0	260 – 400	700 – 780
	$W_3 \rightarrow W_4$ bands	3.0	520 – 800	780 – 830

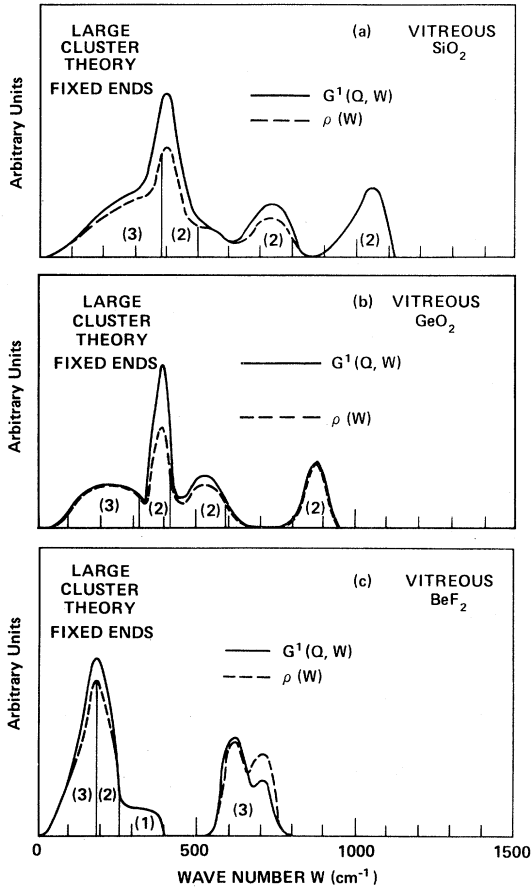


FIG. 27. Division of $\rho(W)$, the theoretical vibrational densities of states of Bell and Dean (Ref. 18), into areas with relative weights (in parentheses) as predicted by the augmented central-force (ACF) model. Thus, in (b), the low-frequency $\frac{3}{9}$ of the states in v - GeO_2 delineate a separate band of largely acoustic nature, the next $\frac{2}{9}$ comprise a rather narrow band of largely rocking nature, and the next two bands each contain $\frac{2}{9}$ of the states that are predicted by the central-force-only model. Minor discrepancies are more likely due to the fixed-ends nature of the cluster model than to an inappropriateness of the admittedly idealized ACF model. See also Figs. 24–26 and Table III.

atoms removes a substantial (and presently uncalculated) number of degrees of freedom (and vibrational modes) from the problem. Nevertheless, the division of $\rho(\omega)$ into bands at approximately $\frac{3}{9}$, $\frac{5}{9}$, and $\frac{7}{9}$ of the states is impressive for the v - GeO_2 theory in Fig. 27(b). We conclude that the ACF model provides a useful simplified picture of the distribution of vibrational states for the large-cluster calculations of Bell *et al.* Moreover, the ACF model suggests a way to partition the VDOS into bands whose areas should be in the ratio of known small integers.

We have applied this procedure to the results of the neutron scattering experiments. Since $\rho(\omega)$ is not directly measured, and since the neutron scattering coupling factor $A(Q, \omega)$ in Eq. (21) is thought to be slowly varying, we have simply integrated the $G^1(Q, \omega)$ curves given in Figs. 5(a), 6(a), and 7(a). The frequencies for $\frac{3}{9}$, $\frac{5}{9}$, $\frac{6}{9}$, and $\frac{7}{9}$ of the total area are listed in the $G^1(Q, \omega)$ column of Table III and are marked on the G^1 curves in Fig. 28. The $\frac{5}{9}$ and $\frac{7}{9}$ frequencies divide the v - SiO_2 and v - GeO_2 spectra

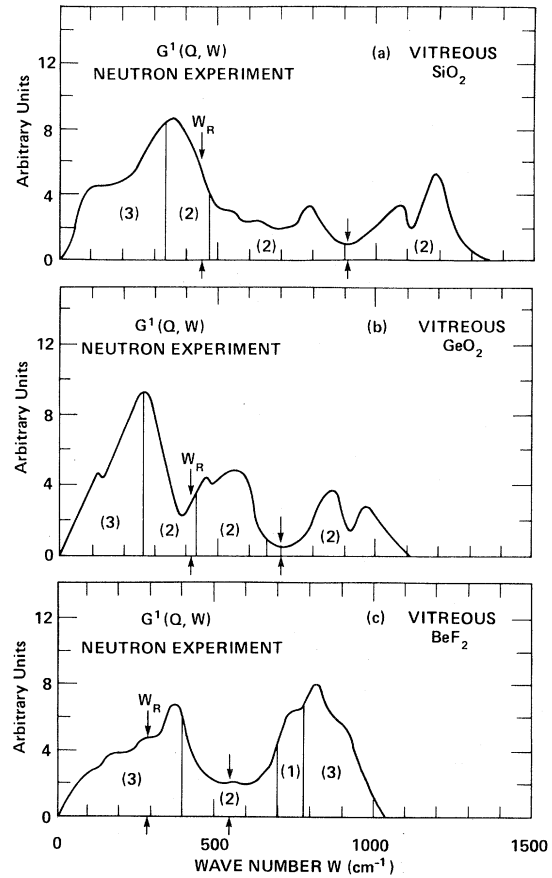


FIG. 28. Division of the experimental estimate of the vibrational density of states approximated by $G_1(Q, W)$ into areas of relative weight as predicted by the augmented central-force model. Correspondence with obvious features is not as good as in Fig. 27 for theoretical state densities, suggesting that the neutron scattering coupling coefficients A in $G_1(Q, W) \cong A(Q, W)\rho(W)$ are relatively small at lower frequencies. The pairs of vertical arrows mark the apparent “natural” separation of bands, at $W_1 = W_R$ (the position of the dominant Raman line) and at the obvious “gap” between groups of states, seen to lie between W_2 and W_3 in Figs. 24–26. The arrows are expected to divide the density of states into groups of predictable relative weights, enabling the empirical estimate of the frequency variation of A given in Table IV.

into groups of bands approximately as anticipated from the ACF model, keeping in mind the TO-LO splitting of the high-frequency modes. The $\frac{6}{9}$ division of the ν -BeF₂ spectrum (at 780 cm⁻¹ in Fig. 28) fails to divide the spectrum into the two distinct groupings anticipated from the ACF and large-cluster models. Inspection of Fig. 28 suggests that the $\frac{6}{9}$ frequency should have been ~ 550 cm⁻¹. This substantial discrepancy may point to significant ω dependence of the coupling coefficients $A(Q, \omega)$ in ν -BeF₂. Were the discrepancy due to underestimation of the two-phonon contribution in Fig. 4(c), the ω dependence of A would likely be even greater.

D. The neutron coupling coefficients

One can use the ACF model to obtain an empirical estimate of the variation of $A(Q, \omega)$ from band to band. Study of Figs. 24–26 reveals two relatively unambiguous dividing points: ω_1 , which is marked experimentally by the position of the dominant Raman line, and the center of the gap between the band edges ω_2 and ω_3 . These frequencies are marked in Fig. 28 by the pairs of vertical arrows, thus dividing the spectra into three regions listed numerically in Table IV. The ACF model, therefore, predicts relative densities of states ρ as shown in Table IV, and integration of the curves in Fig. 28 gives the corresponding partial areas G^1 also shown in the table.

The empirical estimate of the relative coupling coefficient over each range is given by A in the table, according to Eq. (21) and comments in the table caption. We shall discuss these results shortly.

An entirely theoretical estimate of A has been obtained for the corresponding groups of ACF states using the cluster theory curves and dividing frequencies given in Fig. 27. These values are entered in the last column of Table IV. They are obtained by taking the ratio of the areas under the $G^1(Q, \omega)$ and $\rho(\omega)$ curves over the appropriate range [which can be found in the $\rho(\omega)$ column of Table III]. For example, the cluster theory curves for ν -BeF₂ are integrated over the ranges 0–190, 190–400, and 520–800 cm⁻¹, corresponding to the ACF grouping of states in the cluster theory. According to the last column of Table IV, the cluster theory estimates of A are qualitatively similar for all three glasses, decreasing from about 1.35 to 1.00 as band frequencies increase. Figure 27 shows that cluster theory predicts the largest neutron coupling coefficients in the region of the rocking modes [which give the highest peak in the theoretical $G^1(Q, \omega)$].

According to Table IV, the empirical ACF values of the relative coupling coefficients A vary little (<20%) with frequency for ν -SiO₂ and ν -GeO₂. The observed tendency towards enhancement ($A > 1$) at low frequencies is perhaps somewhat weaker than predicted by cluster theory. Considering the approximations involved, one may regard the

TABLE IV. An experimental estimate of the relative coupling coefficients $A(Q, \omega)$ involved in $G^1(Q, \omega) \cong A(Q, \omega)\rho(\omega)$. The wave-number ranges are chosen from the experimental neutron and Raman data as marked by the vertical arrows in Fig. 28, and as explained in the text. The expected fraction of vibrational states in each range ρ is as predicted by the augmented central-force model, and summarized in Figs. 24–26. The observed fractional area G^1 is obtained by integration of the experimental curves in Fig. 28 over the indicated ranges. The resultant average coupling coefficients A are given by G^1/ρ and are then normalized for each material to give $A = 1$ over the highest-frequency band. For SiO₂ and GeO₂, these empirical coupling coefficients are nearly frequency independent, while for BeF₂ they are clearly smaller at low frequencies. The theoretical estimates are obtained in a similar way from Fig. 27, which is based on large-cluster calculations.

Glass	Augmented central-force modes	Wave-number range (cm ⁻¹)	ρ	G^1	A	Corresponding cluster theory
			Expected fraction of states $\times 9$	Observed fraction of area $\times 9$	Empirical coupling coefficient	
SiO ₂	Acoustic and rocking	0 – 450	5.0	4.7	0.94	1.35
	$W_1 \rightarrow W_3$ bands	450 – 910	2.0	2.3	1.15	1.29
	$W_2 \rightarrow W_4$ bands	910 – 1350	2.0	2.0	1.00	1.00
GeO ₂	Acoustic and rocking	0 – 420	5.0	5.0	1.11	1.25
	$W_1 \rightarrow W_3$ bands	420 – 700	2.0	2.2	1.22	1.18
	$W_2 \rightarrow W_4$ bands	700 – 1100	2.0	1.8	1.00	1.00
BeF ₂	Acoustic and rocking	0 – 295	3.0	1.9	0.41	1.41
	$W_1 \rightarrow W_2$	295 – 550	3.0	2.5	0.54	1.38
	$W_3 \rightarrow W_4$ bands	550 – 1030	3.0	4.6	1.00	1.00

two methods of estimating coupling coefficients as in satisfactory agreement for ν -SiO₂ and ν -GeO₂, but not for ν -BeF₂.

According to the ACF analysis, the neutron coupling coefficients for the low-frequency ν -BeF₂ bands (0–400 cm⁻¹) are about 0.5, rather than the approximately 1.4 calculated from Eq. (6) and the cluster theory. This discrepancy is not a fault of the ACF model as such, since Fig. 27(c) shows clearly that the $\rho(\omega)$ of cluster theory assigns precisely the same relative number of states (6 and 3) to the low- and high-frequency groups of bands. The discrepancy seems too large to point to possible omissions in details of the structure (a few fivefold-coordinated Be atoms⁹⁸ or the force-constant model (large β and/or nonzero next-nearest neighbor interactions⁹⁹). It may point to failure in ν -BeF₂ of some of the assumptions leading to Eqs. (5) and (6), or to undetected error in the use of the participation ratios¹⁵ to evaluate those equations for ν -BeF₂. The precise origin of the discrepancy is unknown.

Brawer¹⁰⁰ has recently computed $\rho(\omega)$ and $G^1(Q, \omega)$ for ν -BeF₂ from molecular dynamics simulations of the structure. He finds that $\frac{2}{3}$ of the states are in the low-frequency group, in agreement with $\rho(\omega)$ for the ACF and large-cluster models. His predicted $G^1(Q, \omega)$ has approximately equal area in both groups, in agreement with experiment, and thus supports the ACF empirical estimate of A in Table IV.

VII. CONCLUDING COMMENTS

We have shown that the inelastic neutron scattering spectrum $G(Q, \omega)$ of a glass containing two chemical elements gives a useful measure of the VDOS, at least for the special cases of ν -SiO₂ and ν -GeO₂. We have observed that the HV Raman spectrum mimics the VDOS, and that the dominant line in the HH Raman spectrum marks the low-frequency limit of the bands that are due mainly to central forces. This allows division of the VDOS

into regions whose relative weights are predicted by a simple theory in which central forces are augmented by rocking and acoustic bands (associated with approximate inclusion of noncentral forces). These relative weights agree reasonably well with the results of cluster theory for all three materials and with the neutron experiment on ν -SiO₂ and ν -GeO₂, and thus provide evidence that the neutron scattering coupling coefficients in these materials have only a weak frequency dependence. The frequency dependence appears to be greater in ν -BeF₂.

Several improvements are called for. Intense pulsed neutron sources should enable acquisition of neutron data with better signal-to-noise ratio and resolution for both the present materials and other glasses. Such measurements should be done and compared with Raman and ir data, e.g., to see if the true linewidths in neutron and optical spectra are the same (i.e., to test the accuracy with which various portions of the optical spectra mimic the VDOS). Future calculations of the dynamics of models should not stop with calculation of the VDOS, but should proceed to compute the neutron $G(Q, \omega)$ according to Eqs. (5) and (6) or improved substitutes. This is because all the necessary information [including the eigenamplitudes $U(\omega)$] is accessible during the dynamical calculation, but not afterwards. Success in predicting the relative weights of states using the augmented central-force model suggests efforts to more correctly include noncentral forces in this approach to the problem. The results might then lead to understanding of the selection rule observations for low-frequency Raman and ir response.

ACKNOWLEDGMENTS

The authors are grateful to Dr. A. E. Geissberger for helpful discussion of this paper. The work of F.L.G. is supported by the U.S. Office of Naval Research (G.B. Wright) under Contract No. N00014-80-C-0713. We are also grateful to E. Plowman for careful aid in the preparation of the manuscript.

¹P. Dean, Rev. Mod. Phys. **44**, 127 (1972).

²A. S. Barker, Jr., and A. J. Sievers, Rev. Mod. Phys. **47**, Suppl. 2, 1 (1975).

³D. Weaire and P. C. Taylor, in *Dynamical Properties of Solids*, edited by G. K. Horton and A. A. Maradudin (North-Holland, Amsterdam, 1980), Vol. 4, p. 1.

⁴M. F. Thorpe, in *Vibrational Spectroscopy of Molecular Liquids and Solids*, edited by S. Bratos and R. M. Pick (Plenum, New York, 1980), p. 341.

⁵D. L. Weaire, in *Amorphous Solids*, edited by W. A. Phillips (Springer, Berlin, 1981), p. 13.

⁶J. Jäckle, in *Vibrational Spectroscopy of Molecular Liquids and Solids*, Ref. 4, p. 135.

⁷F. L. Galeener, in *Excitations in Disordered Systems*, edited by M. F. Thorpe (Plenum, New York, 1982), p. 359.

⁸R. J. Bell, Rep. Prog. Phys. **35**, 1315 (1972).

⁹R. J. Bell, in *Methods in Computational Physics*, edited

- by G. Gilat (Academic, New York, 1976), p. 215.
- ¹⁰R. J. Bell, in *Excitations in Disordered Systems*, Ref. 7, p. 333.
- ¹¹R. J. Bell, in *Excitations in Disordered Systems*, Ref. 7, p. 347.
- ¹²R. J. Bell and P. Dean, *Nature (London)* **212**, 1354 (1966).
- ¹³R. J. Bell, N. F. Bird, and P. Dean, *J. Phys. C* **1**, 299 (1968).
- ¹⁴R. J. Bell and P. Dean, in *Localized Excitations in Solids*, edited by R. F. Wallis (Plenum, New York, 1968), p. 124.
- ¹⁵R. J. Bell and P. Dean, *Discuss. Faraday Soc.* **50**, 55 (1970).
- ¹⁶R. J. Bell, P. Dean, and D. C. Hibbins-Butler, *J. Phys. C* **3**, 2111 (1970).
- ¹⁷R. J. Bell, P. Dean, and D. C. Hibbins-Butler, *J. Phys. C* **4**, 1214 (1971).
- ¹⁸R. J. Bell and P. Dean, in *Amorphous Materials*, edited by R. W. Douglas and Bryan Ellis (Wiley-Interscience, London, 1972), p. 433.
- ¹⁹R. J. Bell and P. Dean, *Philos. Mag.* **25**, 1381 (1972).
- ²⁰R. J. Bell, *J. Phys. C* **7**, L265 (1974).
- ²¹R. J. Bell, N. F. Bird, and P. Dean, *J. Phys. C* **7**, 2457 (1974).
- ²²R. J. Bell and D. C. Hibbins-Butler, *J. Phys. C* **8**, 787 (1975).
- ²³R. J. Bell and D. C. Hibbins-Butler, *J. Phys. C* **9**, 1171 (1976).
- ²⁴R. J. Bell and D. C. Hibbins-Butler, *J. Phys. C* **9**, 2955 (1976).
- ²⁵R. J. Bell, A. Carnevale, C. R. Kurkjian, and G. E. Peterson, *J. Non-Cryst. Solids* **35-36**, 1185 (1980).
- ²⁶P. N. Sen and M. F. Thorpe, *Phys. Rev. B* **15**, 4030 (1977).
- ²⁷R. Kulas and M. F. Thorpe, in *Structure and Excitations of Amorphous Solids—1976*, Proceedings of the 1976 Williamsburg Meeting of the Division of Structure and Excitation of Amorphous Solids of the American Physical Society, edited by G. Lucovsky and F. L. Galeener (AIP, New York, 1976), p. 251.
- ²⁸M. F. Thorpe and F. L. Galeener, *Phys. Rev. B* **22**, 3078 (1980).
- ²⁹R. Shuker and R. W. Gammon, *Phys. Rev. Lett.* **25**, 222 (1970).
- ³⁰R. Shuker and R. W. Gammon, in *Light Scattering in Solids*, edited by M. Balkanski (Flammarion, Paris, 1971), p. 334.
- ³¹R. Shuker and R. W. Gammon, *Phys. Lett.* **33A**, 96 (1970).
- ³²R. Shuker and R. W. Gammon, *J. Chem. Phys.* **55**, 4784 (1971).
- ³³F. L. Galeener and P. N. Sen, *Phys. Rev. B* **17**, 1928 (1978).
- ³⁴F. L. Galeener, *Phys. Rev. B* **19**, 4292 (1979).
- ³⁵R. M. Martin and F. L. Galeener, *Phys. Rev. B* **23**, 3071 (1981).
- ³⁶A. J. Leadbetter, *J. Chem. Phys.* **51**, 779 (1969).
- ³⁷A. J. Leadbetter and D. Litchinsky, *Discuss. Faraday Soc.* **50**, 62 (1970).
- ³⁸A. J. Leadbetter and A. C. Wright, *J. Non-Cryst. Solids* **3**, 239 (1970).
- ³⁹A. J. Leadbetter and M. W. Stringfellow, *Neutron Inelastic Scattering* (International Atomic Energy Agency, Vienna, 1974), p. 501.
- ⁴⁰A. J. Leadbetter, A. C. Wright, and A. J. Apling, in *Amorphous Materials*, edited by R. W. Douglas and Bryan Ellis (Wiley-Interscience, London, 1972), p. 423.
- ⁴¹A. C. Wright, in *Advances in Structure Research by Diffraction Methods*, edited by W. Hoppe *et al.* (Interscience, New York, 1974), Vol. 5, p. 1.
- ⁴²A. C. Wright and A. J. Leadbetter, *Phys. Chem. Glasses* **17**, 122 (1976).
- ⁴³M. F. Collins, B. C. Haywood, and G. C. Stirling, *J. Chem. Phys.* **52**, 1828 (1970).
- ⁴⁴W. M. Lomer and G. G. Low, in *Thermal Neutron Scattering*, edited by P. A. Egelstaff (Academic, New York, 1965), p. 2.
- ⁴⁵M. M. Elcombe, *Proc. Phys. Soc. London* **91**, 947 (1967).
- ⁴⁶J. F. Scott and S. P. S. Porto, *Phys. Rev.* **161**, 903 (1967).
- ⁴⁷C. C. Huang and A. Pasternak, *J. Phys. C* **9**, 3925 (1976).
- ⁴⁸F. L. Galeener and G. Lucovsky, *Phys. Rev. Lett.* **37**, 1474 (1976).
- ⁴⁹F. L. Galeener and G. Lucovsky, in *Structure and Excitations of Amorphous Solids—1976*, Ref. 27, p. 223.
- ⁵⁰F. L. Galeener, G. Lucovsky, and R. H. Geils, *Solid State Commun.* **25**, 405 (1978).
- ⁵¹V. N. Denisov, B. N. Mavrin, V. B. Podobedov, and Kh. E. Sterin, *Fiz. Tverd. Tela (Leningrad)* **20**, 3485 (1978) [*Sov. Phys.—Solid State* **20**, 2016 (1978)].
- ⁵²K. Hübner, L. Schumann, A. Lehmann, H. H. Vajen, and G. Zuther, *Phys. Status Solidi B* **104**, K1 (1981).
- ⁵³Obtained from Amersil Inc, 685 Ramsey Avenue, Hillside, New Jersey 07205.
- ⁵⁴F. L. Galeener (unpublished).
- ⁵⁵F. L. Galeener and R. H. Geils, in *The Structure of Non-Crystalline Materials*, edited by P. H. Gaskell (Taylor and Francis, London, 1977), p. 223.
- ⁵⁶R. H. Stolen and G. E. Walrafen, *J. Chem. Phys.* **64**, 2623 (1976).
- ⁵⁷F. L. Galeener, J. C. Mikkelsen, Jr., and N. M. Johnson, in *The Physics of SiO₂ and Its Interfaces*, edited by S. T. Pantelides (Pergamon, New York, 1978), p. 284.
- ⁵⁸J. C. Mikkelsen, Jr. and F. L. Galeener, *J. Non-Cryst. Solids* **37**, 71 (1980).
- ⁵⁹F. L. Galeener and J. C. Mikkelsen, Jr., *Appl. Phys. Lett.* **38**, 336 (1981).
- ⁶⁰J. C. Mikkelsen, Jr., F. L. Galeener, and W. J. Mosby, *J. Electron. Mater.* **10**, 631 (1981).
- ⁶¹Kindly supplied by Dr. R. H. Stolen.
- ⁶²F. L. Galeener, *J. Non-Cryst. Solids* **40**, 527 (1980).
- ⁶³D. A. Long, *Raman Spectroscopy* (McGraw-Hill, New York, 1977).
- ⁶⁴F. A. Jenkins and H. E. White, *Fundamentals of Optics*, 3rd ed. (McGraw-Hill, New York, 1975), Chap. 25.

- ⁶⁵F. L. Galeener, J. C. Mikkelsen, Jr., R. H. Geils, and W. J. Mosby, *Appl. Phys. Lett.* **32**, 34 (1978).
- ⁶⁶F. L. Galeener, in *Light Scattering in Solids*, edited by M. Balkanski, R. C. C. Leite, and S. P. S. Porto (Flammarion, Paris, 1976), p. 641.
- ⁶⁷T. S. Moss, *Optical Properties of Semiconductors* (Academic, New York, 1959), Chap. 2. See also Ref. 3.
- ⁶⁸G. Lucovsky and F. L. Galeener, in *Structure and Properties of Non-Crystalline Semiconductors*, edited by B. T. Kolomiets (Nauka, Leningrad, 1976), p. 207.
- ⁶⁹F. L. Galeener, G. Lucovsky, and R. H. Geils, *Phys. Rev. B* **19**, 4251 (1979).
- ⁷⁰F. L. Galeener, G. Lucovsky, and J. C. Mikkelsen, Jr., *Phys. Rev. B* **22**, 3983 (1980).
- ⁷¹B. Bendow, M. G. Drexhage, P. K. Bannerjee, J. Goltman, S. S. Mitra, and C. T. Moynihan, *Solid State Commun.* **37**, 485 (1981).
- ⁷²F. L. Galeener and J. C. Mikkelsen, Jr., *Solid State Commun.* **30**, 505 (1979).
- ⁷³C. H. Henry and J. J. Hopfield, *Phys. Rev. Lett.* **15**, 964 (1965).
- ⁷⁴E. Burstein, *Comments Solid State Phys.* **1**, 202 (1968).
- ⁷⁵E. Burstein and D. L. Mills, *Comments Solid State Phys.* **2**, 93 (1969).
- ⁷⁶E. Burstein and D. L. Mills, *Comments Solid State Phys.* **2**, 111 (1969).
- ⁷⁷F. L. Galeener, *Solid State Commun.* (in press).
- ⁷⁸F. L. Galeener, *J. Non-Cryst. Solids* **49**, 53 (1982).
- ⁷⁹R. H. Stolen, J. T. Krause, and C. R. Kurkjian, *Discuss. Faraday Soc.* **50**, 103 (1970).
- ⁸⁰J. B. Bates, R. W. Hendricks, and L. B. Shaffer, *J. Chem. Phys.* **61**, 4163 (1974).
- ⁸¹G. N. Greaves, *J. Non-Cryst. Solids* **32**, 295 (1979).
- ⁸²G. Lucovsky, *Philos. Mag.* **39**, 513 (1979).
- ⁸³R. B. Laughlin, J. D. Joannopoulos, C. A. Murray, K. J. Hartnett, and T. J. Greytak, *Phys. Rev. Lett.* **40**, 461 (1978).
- ⁸⁴C. A. Murray and T. J. Greytak, *J. Chem. Phys.* **71**, 3355 (1979); *Phys. Rev. B* **20**, 3368 (1979).
- ⁸⁵E. J. Friebele, D. L. Griscom, M. Stapelbroeck, and R. A. Weeks, *Phys. Rev. Lett.* **42**, 1346 (1979).
- ⁸⁶A. R. Silin and P. J. Bray, *Bull. Am. Phys. Soc.* **26**, 218 (1981).
- ⁸⁷S. W. Barber, in *The Physics of SiO₂ and Its Interfaces*, Ref. 57, p. 284.
- ⁸⁸W. Wadia and L. S. Balloomal, *Phys. Chem. Glasses* **9**, 115 (1968).
- ⁸⁹G. Lucovsky and R. M. Martin, *J. Non-Cryst. Solids* **8-10**, 185 (1972).
- ⁹⁰R. B. Laughlin and J. D. Joannopoulos, *Phys. Rev. B* **16**, 2942 (1977).
- ⁹¹R. B. Laughlin and J. D. Joannopoulos, *Phys. Rev. B* **17**, 2790 (1978).
- ⁹²R. B. Laughlin and J. D. Joannopoulos, *Phys. Rev. B* **17**, 4922 (1978).
- ⁹³For "typical" ring statistics, see A. C. Wright and J. A. Erwin Desa, *Phys. Chem. Glasses* **19**, 140 (1978).
- ⁹⁴M. F. Thorpe, in *Excitations in Disordered Systems*, Ref. 7, p. 85.
- ⁹⁵F. L. Galeener, *J. Phys. (Paris) Colloq.* **42**, C6-24 (1981).
- ⁹⁶F. L. Galeener and J. C. Mikkelsen, Jr., *Phys. Rev. B* **23**, 5527 (1981).
- ⁹⁷See, eg., G. W. Chantry, in *The Raman Effect*, edited by A. Anderson (Marcel Dekker, New York, 1971), Vol. 1, p. 74ff.
- ⁹⁸S. A. Brawer and M. J. Weber, *J. Chem. Phys.* **75**, 3522 (1981).
- ⁹⁹An example might be direct F-F interactions.
- ¹⁰⁰S. A. Brawer (private communication).